Euclid Quick Data Release (Q1)

First *Euclid* statistical study of galaxy mergers and their connection to active galactic nuclei

```
Euclid Collaboration: A. La Marca<sup>®</sup><sup>1,2</sup>, L. Wang<sup>®</sup><sup>1,2</sup>, B. Margalef-Bentabol<sup>®</sup><sup>1</sup>, L. Gabarra<sup>®</sup><sup>3</sup>, Y. Toba<sup>4,5,6</sup>,
 M. Mezcua<sup>67,8</sup>, V. Rodriguez-Gomez<sup>69</sup>, F. Ricci<sup>610,11</sup>, S. Fotopoulou<sup>612</sup>, T. Matamoro Zatarain<sup>612</sup>, V. Allevato<sup>613</sup>,
  F. La Franca<sup>10</sup>, F. Shankar<sup>14</sup>, L. Bisigello<sup>15</sup>, G. Stevens<sup>12</sup>, M. Siudek<sup>16</sup>, W. Roster<sup>17</sup>, M. Salvato<sup>17</sup>, C. Tortora<sup>13</sup>, L. Spinoglio<sup>18</sup>, A. W. S. Man<sup>19</sup>, J. H. Knapen<sup>20</sup>, M. Baes<sup>22</sup>, D. O'Ryan<sup>23</sup>, N. Aghanim<sup>24</sup>,
                 B. Altieri<sup>©23</sup>, A. Amara<sup>25</sup>, S. Andreon<sup>©26</sup>, N. Auricchio<sup>©27</sup>, H. Aussel<sup>©28</sup>, C. Baccigalupi<sup>©29, 30, 31, 32</sup>,
            M. Baldi<sup>©</sup><sup>33, 27, 34</sup>, S. Bardelli<sup>©</sup><sup>27</sup>, P. Battaglia<sup>©</sup><sup>27</sup>, A. Biviano<sup>©</sup><sup>30, 29</sup>, A. Bonchi<sup>©</sup><sup>35</sup>, E. Branchini<sup>©</sup><sup>36, 37, 26</sup>, M. Brescia<sup>©</sup><sup>38, 13</sup>, J. Brinchmann<sup>©</sup><sup>39, 40</sup>, S. Camera<sup>©</sup><sup>41, 42, 43</sup>, G. Cañas-Herrera<sup>©</sup><sup>44, 45, 46</sup>, V. Capobianco<sup>©</sup><sup>43</sup>,
         C. Carbone<sup>647</sup>, J. Carretero<sup>648, 49</sup>, M. Castellano<sup>611</sup>, G. Castignani<sup>627</sup>, S. Cavuoti<sup>613, 50</sup>, K. C. Chambers<sup>651</sup>.
       Cimatti<sup>52</sup>, C. Colodro-Conde<sup>20</sup>, G. Congedo<sup>53</sup>, C. J. Conselice<sup>54</sup>, L. Conversi<sup>55</sup>, Y. Copin<sup>56</sup>, A. Costille<sup>57</sup>,
         F. Courbin<sup>58,59</sup>, H. M. Courtois<sup>60</sup>, M. Cropper<sup>61</sup>, A. Da Silva<sup>62,63</sup>, H. Degaudenzi<sup>64</sup>, G. De Lucia<sup>30</sup>,
        A. M. Di Giorgio 18, C. Dolding 4, H. Dole 24, F. Dubath 64, C. A. J. Duncan 54, X. Dupac 3, A. Ealet 56,
       S. Escoffier<sup>65</sup>, M. Fabricius<sup>17,66</sup>, M. Farina<sup>18</sup>, R. Farinelli<sup>27</sup>, F. Faustini<sup>35,11</sup>, S. Ferriol<sup>56</sup>, F. Finelli<sup>27,67</sup>,
                         M. Frailis<sup>30</sup>, E. Franceschi<sup>27</sup>, S. Galeotta<sup>30</sup>, K. George<sup>66</sup>, B. Gillis<sup>53</sup>, C. Giocoli<sup>27,34</sup>,
       P. Gómez-Alvarez<sup>68,23</sup>, J. Gracia-Carpio<sup>17</sup>, B. R. Granett<sup>26</sup>, A. Grazian<sup>15</sup>, F. Grupp<sup>17,66</sup>, L. Guzzo<sup>69,26,70</sup>,
      S. Gwyn<sup>1</sup>, S. V. H. Haugan<sup>1</sup>, W. Holmes<sup>73</sup>, I. M. Hook<sup>1</sup>, F. Hormuth<sup>75</sup>, A. Hornstrup<sup>1</sup>, P. Hudelot<sup>78</sup>,
     K. Jahnke<sup>979</sup>, M. Jhabvala<sup>80</sup>, B. Joachimi<sup>981</sup>, E. Keihänen<sup>982</sup>, S. Kermiche<sup>965</sup>, A. Kiessling<sup>973</sup>, B. Kubik<sup>956</sup>, M. Kümmel<sup>966</sup>, M. Kunz<sup>983</sup>, H. Kurki-Suonio<sup>984,85</sup>, Q. Le Boulc'h<sup>86</sup>, A. M. C. Le Brun<sup>987</sup>, D. Le Mignant<sup>957</sup>,
       S. Ligori<sup>643</sup>, P. B. Lilje<sup>672</sup>, V. Lindholm<sup>684,85</sup>, I. Lloro<sup>688</sup>, G. Mainetti<sup>686</sup>, D. Maino<sup>69,47,70</sup>, E. Maiorano<sup>27</sup>,
   D. Mansutti<sup>630</sup>, S. Marcin<sup>89</sup>, O. Marggraf<sup>690</sup>, M. Martinelli<sup>611,91</sup>, N. Martinet<sup>57</sup>, F. Marulli<sup>692,27,34</sup>, R. Massey<sup>693</sup>,
             S. Maurogordato<sup>94</sup>, E. Medinaceli<sup>©27</sup>, S. Mei<sup>©95,96</sup>, M. Melchior<sup>97</sup>, Y. Mellier<sup>98,78</sup>, M. Meneghetti<sup>©27,34</sup>, E. Merlin<sup>©11</sup>, G. Meylan<sup>99</sup>, A. Mora<sup>©100</sup>, M. Moresco<sup>©92,27</sup>, L. Moscardini<sup>©92,27,34</sup>, R. Nakajima<sup>©90</sup>,
   C. Neissner <sup>101,49</sup>, S.-M. Niemi <sup>44</sup>, J. W. Nightingale <sup>102</sup>, C. Padilla <sup>101</sup>, S. Paltani <sup>64</sup>, F. Pasian <sup>30</sup>, K. Pedersen <sup>103</sup>, W. J. Percival <sup>104, 105, 106</sup>, V. Pettorino <sup>44</sup>, S. Pires <sup>28</sup>, G. Polenta <sup>35</sup>, M. Poncet <sup>107</sup>, L. A. Popa <sup>108</sup>, L. Pozzetti <sup>27</sup>, F. Raison <sup>17</sup>, R. Rebolo <sup>20, 109,21</sup>, A. Renzi <sup>110,111</sup>, J. Rhodes <sup>73</sup>, G. Riccio <sup>13</sup>, E. Romelli <sup>30</sup>, M. Roncarelli <sup>27</sup>,
    B. Rusholme<sup>112</sup>, R. Saglia<sup>66, 17</sup>, Z. Sakr<sup>113, 114, 115</sup>, D. Sapone<sup>116</sup>, B. Sartoris<sup>66, 30</sup>, J. A. Schewtschenko<sup>53</sup>
  P. Schneider<sup>90</sup>, T. Schrabback<sup>117</sup>, M. Scodeggio<sup>47</sup>, A. Secroun<sup>65</sup>, G. Seidel<sup>79</sup>, M. Seiffert<sup>73</sup>, S. Serrano<sup>8,118,7</sup>, P. Simon<sup>90</sup>, C. Sirignano<sup>110,111</sup>, G. Sirri<sup>34</sup>, L. Stanco<sup>111</sup>, J. Steinwagner<sup>17</sup>, P. Tallada-Crespí<sup>48,49</sup>,
                A. N. Taylor<sup>53</sup>, H. I. Teplitz<sup>119</sup>, I. Tereno<sup>62, 120</sup>, N. Tessore<sup>81</sup>, S. Toft<sup>121, 122</sup>, R. Toledo-Moreo<sup>123</sup>,
   F. Torradeflot 649,48, I. Tutusaus 114, L. Valenziano 77,67, J. Valiviita 84,85, T. Vassallo 66,30, G. Verdoes Kleijn 2,
             A. Veropalumbo<sup>26, 37, 36</sup>, Y. Wang<sup>119</sup>, J. Weller<sup>66, 17</sup>, A. Zacchei<sup>30, 29</sup>, G. Zamorani<sup>27</sup>, F. M. Zerbi<sup>26</sup>,
       I. A. Zinchenko<sup>66</sup>, E. Zucca<sup>27</sup>, M. Ballardini<sup>124, 125, 27</sup>, M. Bolzonella<sup>27</sup>, E. Bozzo<sup>64</sup>, C. Burigana<sup>126, 67</sup>,
R. Cabanaco 114, A. Cappi 27,94, D. Di Ferdinando 34, J. A. Escartin Vigo 17, M. Huertas-Company 20, 16, 127, 128, J. Martín-Fleitas 100, S. Matthew 53, N. Mauri 52, 34, R. B. Metcalf 92, 27, A. Pezzotta 129, 17, M. Pöntinen 84, C. Porciani 90, I. Risso 130, V. Scottez 98, 131, M. Sereno 27, 34, M. Tenti 34, M. Viel 29, 30, 32, 31, 132, M. Wiesmann 72,
                  Y. Akrami<sup>©</sup> <sup>133, 134</sup>, S. Alvi<sup>©</sup> <sup>124</sup>, I. T. Andika<sup>©</sup> <sup>135, 136</sup>, S. Anselmi<sup>©</sup> <sup>111, 110, 137</sup>, M. Archidiacono<sup>©</sup> <sup>69, 70</sup>,
     F. Atrio-Barandela<sup>138</sup>, C. Benoist<sup>94</sup>, K. Benson<sup>61</sup>, D. Bertacca<sup>110</sup>, 15, 111, M. Bethermin<sup>139</sup>, A. Blanchard<sup>114</sup>,
  L. Blot<sup>140, 137</sup>, H. Böhringer<sup>17, 141, 142</sup>, S. Borgani<sup>143, 29, 30, 31, 132</sup>, M. L. Brown<sup>54</sup>, S. Bruton<sup>144</sup>, A. Calabro<sup>11</sup>,
         B. Camacho Quevedo 8, 7, F. Caro 11, C. S. Carvalho 120, T. Castro 30, 31, 29, 132, F. Cogato 92, 27, S. Conseil 56,
    T. Contini<sup>114</sup>, A. R. Cooray<sup>145</sup>, O. Cucciati<sup>27</sup>, S. Davini<sup>37</sup>, F. De Paolis<sup>146</sup>, <sup>147</sup>, <sup>148</sup>, G. Desprez<sup>2</sup>, A. Díaz-Sánchez<sup>149</sup>, J. J. Diaz<sup>20</sup>, S. Di Domizio<sup>36</sup>, <sup>37</sup>, J. M. Diego<sup>150</sup>, P.-A. Duc<sup>139</sup>, A. Enia<sup>33</sup>, <sup>27</sup>, Y. Fang<sup>66</sup>,
           A. G. Ferrari<sup>34</sup>, A. Finoguenov<sup>84</sup>, A. Fontana<sup>11</sup>, F. Fontanot<sup>30, 29</sup>, A. Franco<sup>147, 146, 148</sup>, K. Ganga<sup>95</sup>,
        J. García-Bellido<sup>133</sup>, T. Gasparetto<sup>30</sup>, V. Gautard<sup>151</sup>, E. Gaztanaga<sup>7, 8, 152</sup>, F. Giacomini<sup>34</sup>, F. Gianotti<sup>27</sup>, G. Gozaliasl<sup>153, 84</sup>, M. Guidi<sup>33, 27</sup>, C. M. Gutierrez<sup>154</sup>, A. Hall<sup>53</sup>, W. G. Hartley<sup>64</sup>,
              C. Hernández-Monteagudo<sup>21,20</sup>, H. Hildebrandt<sup>155</sup>, J. Hjorth<sup>103</sup>, J. J. E. Kajava<sup>156,157</sup>, Y. Kang<sup>64</sup>,
```

```
V. Kansal®<sup>158,159</sup>, D. Karagiannis®<sup>124,160</sup>, K. Kiiveri<sup>82</sup>, C. C. Kirkpatrick<sup>82</sup>, S. Kruk®<sup>23</sup>, J. Le Graet®<sup>65</sup>, L. Legrand®<sup>161,162</sup>, M. Lembo®<sup>124,125</sup>, F. Lepori®<sup>163</sup>, G. Leroy®<sup>164,93</sup>, G. F. Lesci®<sup>92,27</sup>, J. Lesgourgues®<sup>165</sup>, L. Leuzzi®<sup>92,27</sup>, T. I. Liaudat®<sup>166</sup>, A. Loureiro®<sup>167,168</sup>, J. Macias-Perez®<sup>169</sup>, G. Maggio®<sup>30</sup>, M. Magliocchetti®<sup>18</sup>, E. A. Magnier®<sup>51</sup>, F. Mannucci®<sup>170</sup>, R. Maoli®<sup>171,11</sup>, C. J. A. P. Martins®<sup>172,39</sup>, L. Maurin®<sup>24</sup>, M. Miluzio<sup>23,173</sup>, P. Monaco®<sup>143,30,31,29</sup>, C. Moretti®<sup>32,132,30,29,31</sup>, G. Morgante<sup>27</sup>, K. Naidoo®<sup>152</sup>, A. Navarro-Alsina®<sup>90</sup>, S. Nesseris®<sup>133</sup>, F. Passalacqua®<sup>110,111</sup>, K. Paterson®<sup>79</sup>, L. Patrizii³<sup>4</sup>, A. Pisani®<sup>65,174</sup>, D. Potter®<sup>163</sup>, S. Quai®<sup>92,27</sup>, M. Radovich®<sup>15</sup>, P.-F. Rocci<sup>24</sup>, S. Sacquegna®<sup>146,147,148</sup>, M. Sahlén®<sup>175</sup>, D. B. Sanders®<sup>51</sup>, E. Sarpa®<sup>32,132,31</sup>, C. Scarlata®<sup>176</sup>, J. Schaye®<sup>46</sup>, A. Schneider®<sup>163</sup>, D. Sciotti®<sup>11,91</sup>, E. Sellentin<sup>177,46</sup>, L. C. Smith®<sup>178</sup>, S. A. Stanford®<sup>179</sup>, K. Tanidis®³, G. Testera³<sup>7</sup>, R. Teyssier®<sup>174</sup>, S. Tosi®³<sup>36,37,26</sup>, A. Troja®<sup>110,111</sup>, M. Tucci<sup>64</sup>, C. Valieri³<sup>34</sup>, A. Venhola®<sup>180</sup>, D. Vergani®<sup>27</sup>, G. Verza®<sup>181</sup>, P. Vielzeuf®<sup>65</sup>, N. A. Walton®<sup>178</sup>, E. Soubrie®<sup>24</sup>, and D. Scott®<sup>19</sup>
```

(Affiliations can be found after the references)

September 12, 2025

ABSTRACT

Galaxy major mergers are indicated as one of the principal pathways to trigger active galactic nuclei (AGN). We present the first statistical analysis of the major merger and AGN connection in the Euclid Deep Fields, and showcase the statistical power of the *Euclid* data. We constructed a stellar-mass-complete ($M_{\star} > 10^{9.8} \, M_{\odot}$) sample of galaxies from the quick data release (Q1) in the redshift range z = 0.5–2. We selected AGN using X-ray detections, optical spectroscopy, and mid-infrared (MIR) colours, and by processing $I_{\rm E}$ observations with an image decomposition algorithm. We used convolutional neural networks trained on cosmological hydrodynamic simulations to classify galaxies as mergers and non-mergers. We found a larger fraction of AGN in mergers compared to the non-merger controls for all AGN selections, with AGN excess factors ranging from two to six. The largest excess we observed was in the MIR AGN. Likewise, a generally larger merger fraction ($f_{\rm merg}$) was seen in active galaxies than in the non-active controls, with the excess depending on the AGN selection method. Furthermore, we analysed $f_{\rm merg}$ as a function of the AGN bolometric luminosity ($L_{\rm bol}$) and the contribution of the point-source component to the total galaxy light in the $I_{\rm E}$ -band ($f_{\rm PSF}$) as a proxy for the relative AGN contribution fraction. We uncovered a rising $f_{\rm merg}$, with an increasing $f_{\rm PSF}$ up to $f_{\rm PSF} \simeq 0.55$, after which we observed a decreasing trend. In the range $f_{\rm PSF} = 0.3$ –0.7, mergers appear to be the dominant AGN fuelling mechanism. We then derived the point-source luminosity ($L_{\rm PSF}$) and showed that $f_{\rm merg}$ monotonically increases as a function of $L_{\rm PSF}$ at z < 0.9, with $f_{\rm merg}$ 50% for $L_{\rm PSF} \simeq 2 \times 10^{43}$ erg s⁻¹. Similarly, at $0.9 \le z \le 2$, $f_{\rm merg}$ rises as a function of $L_{\rm PSF}$, though mergers do not dominate until $L_{\rm PSF} \simeq 10^{45}$ erg s⁻¹. For the X-ray and spectroscopically detected AGN, we derived t

Key words. Galaxies: interactions - Galaxies: evolution - Galaxies: active - Galaxies: statistics

1. Introduction

Galaxy mergers have long been considered a key driver of galaxy evolution, as they have the potential to significantly influence the growth and properties of both host galaxies and their central supermassive black holes (SMBHs; Sanders et al. 1988; Marconi et al. 2004). During such encounters, tidal forces can lead to gas inflows towards central regions (Barnes & Hernquist 1996), that feed intense nuclear star formation and active galactic nucleus (AGN) activity (e.g., Springel et al. 2005; Somerville & Davé 2015; Blumenthal & Barnes 2018). Consequently, this process can trigger AGN feedback, which can severely affect the evolution of a galaxy, for example, by driving galactic-scale outflows and suppressing or enhancing star formation (e.g., Fabian 2012; Harrison et al. 2018). Understanding the connection between mergers and AGN is therefore crucial for advancing our knowledge of galaxy evolution and the formation of large-scale structures (Alexander & Hickox 2012; Heckman & Best 2014).

Previous studies have generally shown that mergers can trigger AGN activation; however, the exact mechanisms driving this process remain poorly understood. While many simulation-based studies have suggested that mergers fuel SMBH accretion and initiate the AGN phase (e.g., Hopkins et al. 2008; Blecha et al. 2018), other simulations propose that mergers serve only

as a secondary fuelling mechanism (e.g., Di Matteo et al. 2003; Martin et al. 2018; Byrne-Mamahit et al. 2023). Similarly, mixed results have also emerged from observations. For example, multiple observational studies have reported a clear link between mergers and AGN triggering (Lackner et al. 2014; Kocevski et al. 2015; Goulding et al. 2018; Ellison et al. 2019; Gao et al. 2020; Toba et al. 2022; Tanaka et al. 2023; Bickley et al. 2024), with a possible dependency on AGN luminosity (Treister et al. 2012; Weigel et al. 2018; Pierce et al. 2022; La Marca et al. 2024), dust obscuration (Ricci et al. 2017, 2021; Donley et al. 2018), and environment (Koulouridis et al. 2006, 2024). However, other studies have highlighted that mergers are a less significant mechanism, being outnumbered by secular processes (Grogin et al. 2005; Allevato et al. 2011; Draper & Ballantyne 2012; Marian et al. 2019; Silva et al. 2021; Smethurst et al. 2024; Garland et al. 2023; Villforth 2023; Bichang'a et al. 2024). Additionally, in several studies, there has been no observed dependence on AGN luminosity (Hewlett et al. 2017; Villforth et al. 2017; Comerford et al. 2024).

The AGN triggering debate could arise from several factors. First, there are various methods to identify mergers, each with its advantages and limitations. Among the different methods, visual classification (Darg et al. 2010), close spectroscopic pairs (Knapen et al. 2015), and non-parametric morphological statistics (Nevin et al. 2019) have been widely employed in the past.

^{*} e-mail: a.la.marca@sron.nl

More recently, several studies have favoured machine learning (ML), in particular deep learning (DL), techniques (e.g., Wang et al. 2020). These methods are reproducible, and once trained, they can process large samples efficiently (for a review, see Margalef-Bentabol et al. 2024a). However, their performance depends on the specific task and is constrained by the quality of the training labels. Second, as in merger detections, there is no unique method to identify AGN. Since AGN exhibit a diverse range of observational signatures and different characteristics of ongoing activity, they can be selected through a multitude of techniques, including X-ray detections, optical emission line ratios, variability, mid-infrared (MIR) colours, and radio emission (for a review, see Heckman & Best 2014). As a result, different selection methods can lead to AGN and host galaxy samples with very different characteristics (Silverman et al. 2008; Hickox & Alexander 2018). For these reasons, a panchromatic approach has emerged in order to properly investigate the merger and AGN connection, accounting for different AGN types (Li et al. 2023).

La Marca et al. (2024) exploited a large multi-wavelength dataset at z < 1 and estimated the AGN contribution fraction parameter, which measures the AGN light contribution to the total galaxy light, through spectral energy distribution (SED) modelling in the rest-frame wavelength range 3–30 µm. The AGN were selected with multiple diagnostics, that is, X-ray, MIR, and SED modelling and a relation was proposed between the merger fraction and the AGN fraction relation, which revealed two distinct regimes. When the AGN is not dominant (low AGN fraction), the fraction of mergers stays roughly constant, with mergers representing only a secondary AGN triggering mechanism. However, for very dominant AGN, where the AGN fraction exceeds 0.8, the merger fraction rises rapidly towards 100%. A similar picture was observed in the merger fraction as a function of the AGN bolometric luminosity. These findings could explain some of the conflicting results in the literature. Secular processes may be the principal fuelling mechanisms in non-dominant and relatively faint AGN, while major mergers are the main or only viable channel to trigger the most powerful and dominant AGN.

So far, a lack of large survey data at high redshift has limited our understanding of the merger and AGN relation and its evolution. To improve our knowledge, particularly at earlier epochs, several key ingredients are needed, including deep imaging data with high spatial resolution to perform morphological classification, large volumes to construct large statistical samples, and multi-wavelength coverage to reliably select a diverse sample of AGN and derive physical properties of AGN and their host galaxies. The advent of *Euclid* and the associated ancillary data finally offers the opportunity to investigate this problem throughout cosmic history up to 'cosmic noon'. Euclid is a European Space Agency (ESA) mission (Laureijs et al. 2011) whose aim is to observe almost all of the extra-Galactic sky with two surveys. Its scientific objectives are outlined in Euclid Collaboration: Mellier et al. (2025). Euclid operates in the optical and near-IR in four bands (I_E , Y_E , J_E , and H_E), covering wavelengths from 0.53 µm to 2.02 µm, (Euclid Collaboration: Cropper et al. 2025; Euclid Collaboration: Jahnke et al. 2025). Although Euclid was designed as a cosmology mission, it will be able to detect billions of sources, of which at least 10 million are expected to be AGN detected in I_E (Euclid Collaboration: Bisigello et al. 2024; Euclid Collaboration: Selwood et al. 2025) and hundreds of thousands in the near-IR bands (Euclid Collaboration: Lusso et al. 2024). This will dramatically increase the number of known AGN with high-resolution imaging, and provide an unprecedented opportunity to study the role of mergers in the evolution of AGN.

The aim of this study is to investigate the connection between mergers and AGN using the first quick release of Euclid data (Euclid Quick Release Q1 2025, hereafter Q1). We constructed a stellar mass-complete sample of galaxies across the redshift range $0.5 \le z \le 2$, with multi-wavelength data ranging from the X-ray to the MIR. We revisited two facets of the merger and AGN connection: i) Using a binary active-non-active AGN classification, we analysed whether mergers are a viable path to trigger AGN and assessed their significance, and ii) exploring continuous AGN properties, we studied how the fraction of mergers varies with AGN dominance and absolute power. Specifically, we explored whether galaxies hosting the most dominant and luminous AGN are more likely to be mergers. We developed a convolutional neural network (CNN) to identify mergers in Euclid I_E images. To mitigate issues with visual classifications, we trained the CNN on mock Euclid observations generated from cosmological hydrodynamic simulations, which include galaxy merger histories. We used four different diagnostics to select AGN and characterised each AGN based on the central point source luminosity relative to the host galaxy and, when possible, its bolometric luminosity.

The paper is organised as follows. In Sect. 2, we first introduce the Euclid data products we use in this work, the ancillary multi-wavelength data, and our galaxy sample selection. Then, we describe the mock Euclid observations generated from cosmological hydro-dynamical simulations to train our DL classifier. In Sect. 3, we present our galaxy merger classifier and the various AGN selection methods adopted. In Sect. 4, we first explore the merger and AGN connection using a binary classification of AGN and non-AGN. Next, we analyse this connection using continuous parameters that characterise the relative and absolute AGN power. We discuss possible caveats in our analysis in Sect. 5. Finally, we summarise our main findings in Sect. 6. Throughout the paper, unless otherwise stated, we assume a flat Λ CDM Universe with $\Omega_{\rm m}=0.3,\,\Omega_{\Lambda}=0.7,$ and $H_0 = 70 \,\mathrm{km \, s^{-1} \, Mpc^{-1}}$ and express magnitudes in the AB system (Oke & Gunn 1983).

2. Data

In this section, we first describe the *Euclid* data. Then, we present a brief description of the multi-wavelength ancillary data, from the X-ray to the MIR. Finally, we introduce the mock *Euclid* VIS imaging data generated from the simulations.

2.1. Euclid data

This work focuses on exploring Q1, comprising data from a single visit of the Euclid Deep Fields (EDFs), namely the EDF North (EDF-N), the EDF South (EDF-S), and the EDF Fornax (EDF-F), covering a total area of $\sim 63 \deg^2$. All EDFs have been observed in all four *Euclid* photometric bands, that is $I_{\rm E}$, $Y_{\rm E}$, $J_{\rm E}$, and $H_{\rm E}$. These observations have been complemented by ground-based optical photometry taken with various instruments across the wavelength range 0.3–1.8 μ m. Q1 includes imaging, spectroscopic data, and value-added catalogues, including photometric redshifts (photo-z; Euclid Collaboration: Tucci et al. 2025). Further details on Q1 can be found in Euclid Collaboration: Aussel et al. (2025), Euclid Collaboration: McCracken et al. (2025), Euclid Collaboration: Polenta et al. (2025), and Euclid Collaboration: Romelli et al. (2025). All *Euclid* data used in this work, catalogues and images, have been retrieved using the ESA Datalabs facility (Navarro et al. 2024).

Catalogues. We selected a sample of galaxies from the *Euclid* MER catalogue (Euclid Collaboration: Altieri et al. in prep.) removing possible contaminants using the available columns as follows. First, we required a VIS $I_{\rm E}$ detection by imposing VIS_DET = 1. Then, we applied the condition DET_QUALITY_FLAG < 4 to filter out contaminants such as bad pixels, saturation, proximity to image borders, location within VIS or NIR bright star masks, presence within extended object areas, or omission by the deblending algorithm due to large pixel size. Additional flags can be used to filter out further contaminants, such as the SPURIOUS_FLAG, which identifies spurious sources. We set this flag to 0 to exclude such sources from our sample. Finally, we applied constraints on source flux and size by imposing MUMAX_MINUS_MAG > -2.6 to filter out point-like sources and 23.9 - 2.5 $\log_{10}(\text{FLUX_DETECTION_TOTAL})$ < 23.5 to exclude faint objects.

In addition to the photometric catalogue, we queried the official pipeline photo-z and stellar masses for each source (Euclid Collaboration: Tucci et al. 2025). We excluded objects flagged (greater than or equal to one) by PHZ_FLAGS, PHYS_PARAM_FLAGS, or QUALITY_FLAG. When available, we used photometric redshifts and stellar masses estimated by Euclid Collaboration: Enia et al. (2025), which complemented the Euclid data with public IRAC observations for an improved quality of the recovered parameters. Finally, we limited our selection to galaxies within the redshift range $0.5 \le \text{photo-}z \le 2.0$ and with stellar mass $M_{\star}/M_{\odot} > 10^{9.8}$. These galaxy parameters are given with their probability distributions and a set of possible values, from which we adopted the median values when applying these selections. The cut on stellar mass is motivated by our requirement of selecting a stellar mass complete sample, since Euclid Collaboration: Enia et al. (2025) showed that at z = 2 the Euclid galaxy sample is 90% complete at $M_{\star}/M_{\odot} \gtrsim 10^{9.8}$, based on the Pozzetti et al. (2010) methodology.

Images. For our task of identifying mergers, we utilised VIS imaging data, which have a pixel resolution of 0".1 and a signal-to-noise ratio $S/N \ge 10$ at $I_E \le 24.5$ (Euclid Collaboration: Cropper et al. 2025). For each galaxy in the selected sample, we made an $8'' \times 8''$ (corresponding to a 80×80 pixel grid) thumbnail centred on the source. This size approximately corresponds to a physical scale of $50 \text{ kpc} \times 50 \text{ kpc}$ in the redshift range considered. We excluded sources for which generating an $8'' \times 8''$ cutout was not feasible because they are at the edge of the field. Additionally, we retrieved the VIS point spread function (PSF), which was used when constructing the training dataset.

Ancillary data. Q1 is complemented by ancillary multiwavelength datasets from photometric surveys, including Xray data from XMM-Newton, Chandra and eROSITA (Euclid Collaboration: Roster et al. 2025, hereafter RW25, and references therein), GALEX (Galaxy Evolution Explorer; Bianchi et al. 2017), Hyper Suprime-Cam (HSC; Miyazaki et al. 2018), Gaia (Gaia Collaboration et al. 2016), UNIONS (Ultraviolet Near-Infrared Optical Northern Survey; Gwyn et al. in prep.), DES (Dark Energy Survey; The Dark Energy Survey Collaboration 2005), the Dark Energy Spectroscopic Instrument (DESI; DESI Collaboration et al. 2016, 2022) Legacy Imaging Surveys (Dey et al. 2019) and spectroscopic survey, and the WISE-AllWISE DR6 survey data (Wright et al. 2010). To create multiwavelength catalogues for each one of the EDFs, Euclid Collaboration: Matamoro Zatarain et al. (2025, hereafter MZ25) performed positional matches with the external surveys using the software STILTS, version 3.5–1 (Taylor 2006). The matching process was customised for each EDF to account for differences in sky coverage. For detailed information on the matching proce-

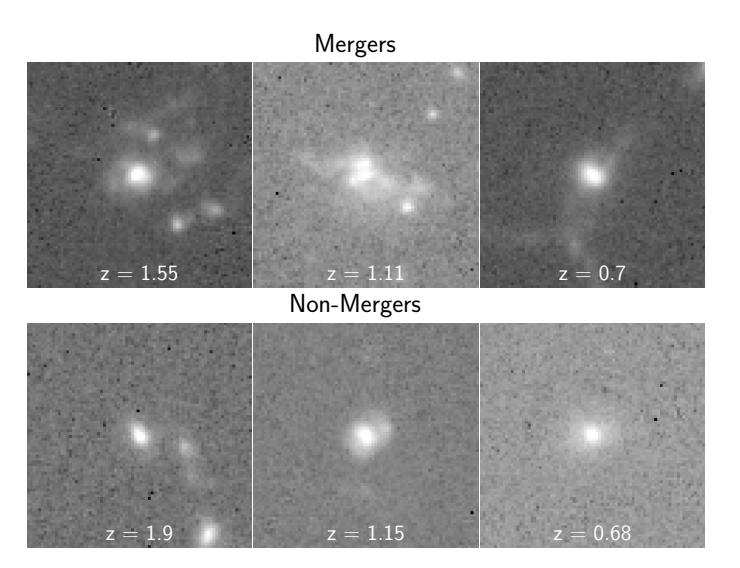


Fig. 1. Examples of mock *Euclid* VIS $I_{\rm E}$ -band observations of TNG galaxies. Galaxies were randomly selected among the TNG100 galaxies available. The images are $8'' \times 8''$ wide and log-scaled in the 1st–99th percentile range. The redshift of each galaxy is reported in each panel.

dure, including the radii used and selection criteria applied, we refer the reader to MZ25.

2.2. The IllustrisTNG galaxy sample

To train our merger identification model, we used simulated galaxies from the IllustrisTNG (hereafter TNG) cosmological hydrodynamical simulations, which provide detailed merger histories in large cosmological volumes, ensuring a large sample of galaxies. The TNG simulation consists of three different volumes varying in physical size and mass resolution (Marinacci et al. 2018; Naiman et al. 2018; Nelson et al. 2018; Pillepich et al. 2018; Springel et al. 2018). We used the TNG100 and TNG300 boxes (hereafter referred to as the TNG simulation), with their box size corresponding to 110.7 Mpc and 302.6 Mpc, respectively. The baryonic matter resolution is $1.4 \times 10^6 \, M_{\odot}$ in TNG100 and $1.1 \times 10^7 M_{\odot}$ in TNG300. Using both TNG suites allows us to confidently select galaxies down to $M_{\star}/M_{\odot} = 10^9$ in TNG100, and to have a large sample of galaxies thanks to the TNG300 size. We required a minimum of about 1000 baryonic particles, which, for TNG100, correspond to galaxies with stellar mass $M_*/M_{\odot} \ge 10^9$, while for TNG300 the lower mass limit is $M_*/M_{\odot} > 8 \times 10^9$.

We selected galaxies within the redshift range z = 0.5-2, corresponding to simulation snapshot numbers 67–33. The time step between each snapshot is 150 Myr. For each galaxy, the TNG simulation provides a complete merger history (Rodriguez-Gomez et al. 2015) identified through the Subfind algorithm (Springel et al. 2001). We then define a subhalo as a merger if a merger event occurred in the previous 300 Myr or will occur within the next 800 Myr. Otherwise, the subhalo is considered a non-merger. This time window is motivated by simulation studies (e.g., Moreno et al. 2019), which show that during this period, the majority of gas is transferred between galaxies, leading to enhanced star formation and nuclear activity. Here we considered only major merger events, with a stellar mass ratio $M_1/M_2 \le 4$. This selection includes pre-mergers (close galaxy pairs expected to merge within 800 Myr), ongoing mergers, and recent postmergers. As such, we sample a significant fraction of the merger timescale, covering the late stages of the dynamical interaction

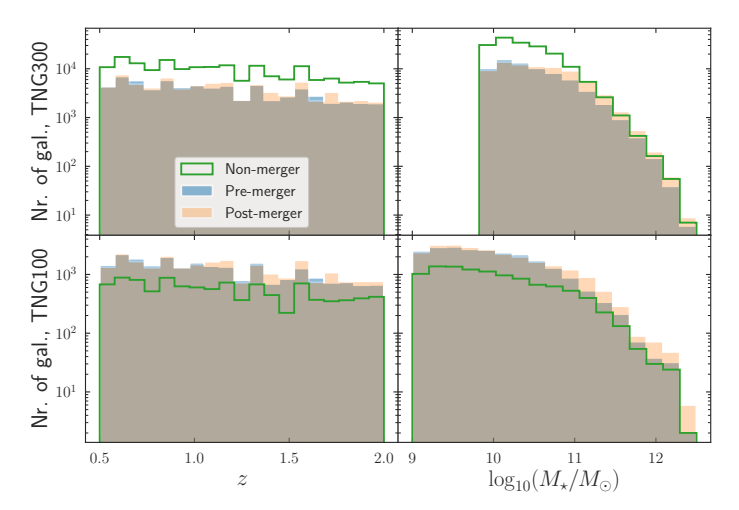


Fig. 2. Redshift (left column) and M_{\star} (right column) distributions for pre-, post-, and non-merging galaxies in the TNG300 (top row) and TNG100 (bottom row) training sets.

and the immediate aftermath of coalescence, but excluding wide pairs that are still in the early interaction phase. It is important to note that the merger rate and its evolution in hydrodynamical simulations such as TNG depend on the underlying galaxy-halo connection implemented in the simulation. Different simulations with distinct prescriptions for galaxy formation physics can yield different merger rates (e.g., Grylls et al. 2020).

The dataset was divided into training, validation, and testing sets, corresponding to 80%, 10%, and 10% of the total sample, respectively. We ensured that galaxies involved in the same merger sequence were included in only one subset. These datasets result in 499 523 galaxies for the training sample (427 577 from TNG300 and 71 946 from TNG100), 54 911 for the validation set (46 660 from TNG300 and 8251 from TNG100), 61 697 for the testing set (52 875 from TNG300 and 8822 from TNG100). Of these, 250 142, 26 999, and 30 986 are mergers, respectively. In each set, we balanced the number of non-mergers with that of mergers. Figure 2 displays the z and M_{\star} distributions of the training samples, split in pre-, post-, and non-mergers.

We generated mock observations for the TNG galaxies following the Margalef-Bentabol et al. (2024a) methodology. We prepared the mock VIS I_E -band observations, at the same pixel resolution of 0".1, as follows:

- Each stellar particle contributes to the galaxy's SED, determined by its mass, age, and metallicity. These SEDs are derived from the stellar population synthesis models of Bruzual & Charlot (2003). The summed SED was passed through the VIS filter to generate a smoothed 2D projected map (Rodriguez-Gomez et al. 2015). The image is then cropped to 8" × 8", corresponding to approximately 50 kpc × 50 kpc in the relevant redshift range, matching the size used for the Euclid galaxy images.
- Each image was convolved with a VIS PSF, randomly chosen to account for the spatial variation of the PSF across the field of view.
- 3. Poisson noise was added to each image to simulate the statistical variation in photon emission from sources over time.
- 4. To ensure realistic merger classifications, it was essential to include observational effects (e.g., Huertas-Company et al. 2019; Rodriguez-Gomez et al. 2015). We injected the TNG galaxies into actual *Euclid* sky cutouts of 8"×8". To prepare

the sky cutouts, we generated random coordinates within the area covered by Q1 data. We controlled the segmentation map for each coordinate, ensuring that within a $9'' \times 9''$ box, all pixels were set to zero¹. When creating the cutouts, we controlled that there were no invalid pixels (NaN values) and that the selected coordinates allowed for a perfectly square cutout without intersecting the edge of a tile.

To create a training sample that accounts for possible AGN, we added a central point source to the host galaxies. The central source intensity can be defined in relation to the host galaxy flux, given the PSF fraction (f_{PSF}):

$$f_{\rm PSF} = \frac{F_{\rm PSF}}{F_{\rm host} + F_{\rm PSF}} \,, \tag{1}$$

where $F_{\rm PSF}$ and $F_{\rm host}$ are the fluxes within a 0".5 aperture of the central source and the host galaxy, respectively. The observed VIS PSF models were used as the central point source. The $f_{\rm PSF}$ values were uniformly chosen in the range 0–1. This operation was performed for a randomly selected 20% of the TNG sample. We show examples of the final mock observations in Fig. 1. To see the effect of each step in the mock observations generation, we refer the reader to Margalef-Bentabol et al. (2024a).

Our mock images do not include dust attenuation, which may affect morphologies at z=2, where the $I_{\rm E}$ -band probes the restframe ultraviolet. However, previous studies have shown that including dust attenuation via full radiative transfer calculations yields only modest changes in the overall classification performance (Bottrell et al. 2019; Rodriguez-Gomez et al. 2019; Wang et al. 2020), while being computationally prohibitive at the scale of our training sample. Moreover, modelling the effect of dust involves many assumptions (e.g. on dust composition and distribution), whose validity remains to be tested (Zanisi et al. 2021). We therefore followed previous works and used dust-free mock observations.

We normalised each image following Bottrell et al. (2019). This normalisation ensures that all images are in a hyperbolic arcsin scale within the range 0–1, maximising the contrast of the central target. A summary of the main steps applied is provided below (see Bottrell et al. 2019, for a detailed description).

- i) We took the hyperbolic arcsin of the images. Values below -7 were converted to NaNs.
- ii) We computed the median of each image, a_{min} , and the 99th percentile, a_{max} , considering a central box of side 25 pixels.
- iii) All values below a_{\min} were set to a_{\min} , including the NaNs. Values above a_{\max} were set to a_{\max} . The resulting clipped images were normalised by subtracting a_{\min} and dividing by $a_{\max} a_{\min}$.

This mock *Euclid* dataset was used to train, validate, and test our merger classifier, as described in the next section.

3. Methodology

Here, we present the DL classifier developed to identify mergers in *Euclid* images. Then, we describe the diagnostics used to select AGN.

3.1. Merger classification using CNNs

We developed a CNN (Lecun et al. 1998) to classify mergers and non-mergers. CNNs consist of multiple layers that apply

¹ This constraint ensures that there are no detected sources or artefacts in each image pixel. The 9" radius is derived from the estimated source density of the EDFs.

Table 1. Convolutional neural network architecture.

Input 0 (1,80,80) Convolutional 32 filters (7,7) 1600 (32,80,80) "same" ReLUMAR Pooling Max Pooling 0 (32,40,40) pool	s stride, padding, U act. size 2
Convolutional 32 filters (7,7) 1600 (32,80,80) "same" ReLU Max Pooling 0 (32,40,40) pool	padding, U act. size 2
Convolutional 32 filters (7,7) 1600 (32,80,80) "same" ReLU Max Pooling 0 (32,40,40) pool	padding, U act. size 2
)%
Dropout 0 (32,40,40) 30	
	c stride
	padding, U act.
	size 2
r	0%
Batch Norm. 256 (64,20,20)	
Convolutional 401 536 (128,20,20) "same"	s stride, padding, U act.
Max Pooling 0 (128,10,10) pool	size 2
Dropout 0 (128,10,10) 30)%
Convolutional 802 944 (128,10,10) "same"	s stride, padding, U act.
Max Pooling 0 (128,5,5) pool	size 2
Dropout 0 (128,5,5) 30)%
Flatten 0 (32 000)	
Dence X10/156 (256)	units, U act.
Dropout 0 (256) 30)%
Dance 37 806 (178)	units, U act.
Dropout 0 (128) 30)%
Dence 120 (1)	ınit, oid act.

Notes. The columns are the name of the Keras layer (and the filters for the convolutional layers), the number of trainable parameters, the output shape, and the hyper-parameters for each layer.

learnable filters to an input image to capture features such as edges and textures. The later layers of the network are typically fully connected, combining the features from earlier layers to calculate a classification for the input image. The architecture developed in this work is presented in Table 1, for which we utilised the Keras framework for the TensorFlow platform (Chollet 2023; Abadi et al. 2016). The CNN consists of four convolutional layers and three fully connected layers. For all layers, we adopted a rectified linear unit (ReLU) as an activation function, except for the final layer, where a sigmoid activation function was used. A stride of one pixel was used for the convolutional layers. We introduced dropout layers after each processing layer to prevent overfitting. These dropout layers randomly set input units to zero at a specified rate. To further prevent overfitting, early stopping in the training phase was used. The specific hyper-parameters, listed in Table 1, include filter numbers and sizes, dropout rates, and strides, chosen based on a grid search.

We evaluated the model performance on the test set from the TNG simulations, using common metrics such as 'precision', 'recall', and 'F1-score'. Precision measures how often the model correctly predicts a given class, while recall focuses on how complete the model is at finding objects in a given class. In other words, precision is the number of objects correctly recovered for a class divided by the total number of objects predicted in that class. Recall is the number of objects correctly recovered

Table 2. Overall performance of the CNN on the TNG test set.

Class	Precision	Recall	F1-score
Mergers	0.80	0.68	0.74
Non-mergers	0.72	0.83	0.77

Notes. Two thresholds were used for classifying galaxies as mergers (score ≥ 0.59) and non-mergers (score < 0.35).

for a class divided by the total number of objects in that class. F1-score is the harmonic mean of precision and recall. All metrics are calculated on a balanced sample (50% mergers and 50% non-mergers).

In this work, we are interested in selecting a pure sample of mergers. Hence, we followed La Marca et al. (2024) to have a higher classification precision for mergers. We searched for a threshold which maximises the F1-score to identify mergers while maintaining a precision greater than or equal to 0.80 for the merger class. According to these prescriptions, the best threshold for mergers is 0.59. Thus, all galaxies with a predicted score greater than 0.59 are classified as mergers. Similarly, to select a sample of non-mergers with low contamination levels, we searched for a threshold that ensures at least 0.70 precision for non-mergers, maximising the F1-score. We lowered the precision to 0.70, given the poorer precision of our classifier for the non-merger class. It is important to highlight that the expected number of non-mergers is much larger than that of interacting galaxies (e.g., Ferreira et al. 2020). Therefore, in real galaxies, we expect a much lower contamination of mergers in predicted non-mergers. The set threshold is 0.35, meaning all galaxies with a predicted score below 0.35 are labelled as non-mergers. Performance metrics for mergers and non-mergers are shown in Table 2. Setting a larger threshold for mergers and a lower one for non-mergers will further improve the purity of both classes, but also strongly affect their completeness, limiting the sample size of both classes.

The model performance is comparable to the performance of other recent studies. Margalef-Bentabol et al. (2024a) benchmarked several state-of-the-art methods to identify major mergers in astronomical images out to z = 1. Each model was trained on mock observations from cosmological hydrodynamical simulations, where mergers have been defined in a similar fashion to this work. Based on the performance metrics on the TNG-test set, the best model in Margalef-Bentabol et al. (2024a, Table 3) obtained a precision of 0.80 and a recall of 0.74 (F1-score 0.77) for the merger class, which is consistent with the performance for mergers we report in Table 2. While comparable to similar contemporary works, the model performance metrics (Table 2) indicate non-negligible levels of sample contamination and incompleteness inherent to automated classification. We quantitatively assess the impact of these classification uncertainties on our key scientific results regarding the merger-AGN connection in Section 5.3.

The *Euclid* collaboration also provides detailed morphologies (Euclid Collaboration: Walmsley et al. 2025), including possible companions and merger features, based on predictions from the Bayesian DL classifier Zoobot (Walmsley et al. 2022). However, these predictions are limited to the top 1% brightest and most extended galaxies, with the selection criteria being segmentation_area > 1200 pixels OR $I_{\rm E}$ < 20.5 mag AND segmentation_area > 200 pixels. In comparison, our stellar mass-complete sample goes down to $I_{\rm E} \simeq 23.5$ mag. Therefore, we developed our own classifier. We compare our model predic-

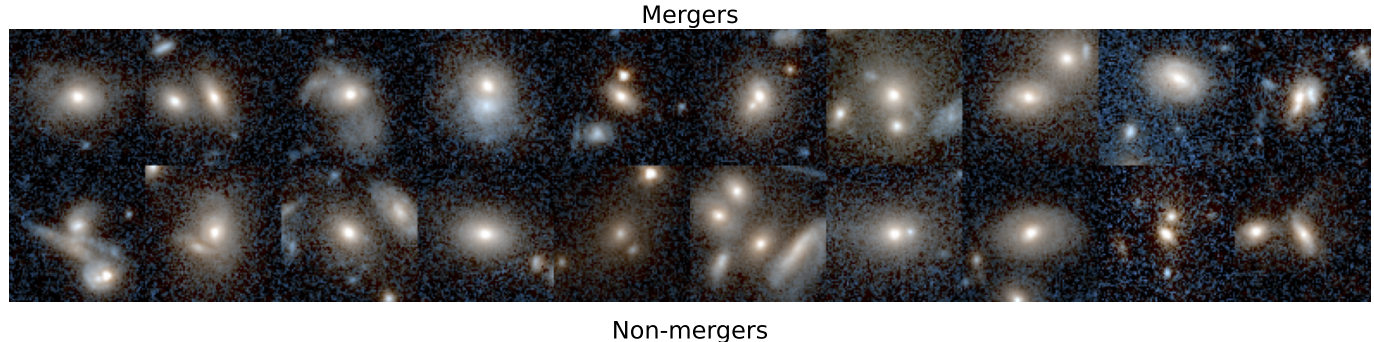




Fig. 3. Examples of galaxies classified as mergers (*top panel*) and as non-mergers (*bottom panel*) by our algorithm. The cutouts are *Euclid* composite RGB images where the R channel is Y_E , the B channel is I_E , and the G channel is the mean, following a 99.85th percentile clip and an arcsinh stretch (x' = arcsinh Qx, with Q = 100; Euclid Collaboration: Walmsley et al. 2025).

tions with the Zoobot classification for the common galaxies in Appendix A.

The double threshold approach has the side effect of producing unclassified galaxies, defined as those with a predicted score between 0.35 and 0.59, inclusive. However, given the large sample size of Q1, this does not affect the analysis carried out in this work. The *Euclid* galaxy sample constructed contains 105 037 sources classified as mergers, 254 564 as non-mergers, and 204 082 unclassified objects. These values correspond to 18.6%, 45.2%, and 36.2% shares of the whole sample, respectively. The catalogue with the merger classification is available from Zenodo². Hereafter, we focus on the classified galaxies and calculate merger fractions as

$$f_{\text{merg}} = \frac{N_{\text{merger}}}{N_{\text{classified}}} = \frac{N_{\text{merger}}}{N_{\text{merger}} + N_{\text{non-merger}}},$$
 (2)

unless differently stated. We show some randomly selected *Euclid* merger and non-merger examples in Fig. 3. Examples of unclassified galaxies are provided in Appendix B. Most galaxies classified as mergers are pair galaxies, with close companions clearly visible in the images. In comparison, non-merger galaxies appear to be quite regular and isolated. Here, we point out that two close galaxies, if both detected, were considered individually rather than as a single system.

3.2. AGN identification

The Q1 data are accompanied by a set of multi-wavelength catalogues that allow for multiple AGN selections. This work focuses on four main AGN detection techniques: X-ray, optical spectroscopy, DL-based image decomposition, and MIR colours. The first *Euclid* AGN catalogue is presented in MZ25 and includes all these AGN selections, except the DL-based image decomposition method, described in Euclid Collaboration:

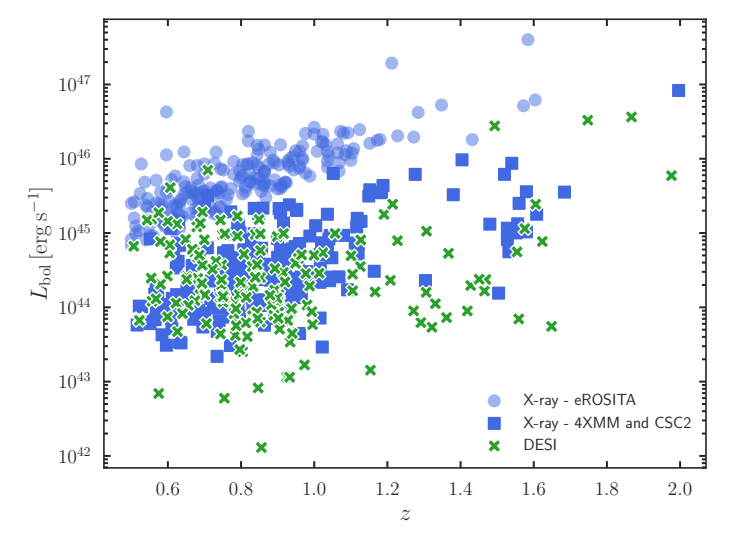


Fig. 4. AGN bolometric luminosity (L_{bol}) versus redshift for the X-ray and DESI-selected AGN.

Margalef-Bentabol et al. (2025, hereafter MB25). The AGN-selection techniques are detailed in these two papers. Here, we summarise the main aspects of the criteria used.

MIR colour selections defined in Assef et al. (2018, hereafter A18). MZ25 used two different diagnostics, C75 and R90, to select MIR AGN among the sources with AllWISE fluxes. The C75 selection, focusing on achieving 75% completeness, is defined as

$$W_1 - W_2 > 0.71 \text{ Vega mag}$$
, (3)

while the R90 diagnostic, optimised for obtaining 90% reliability, is

$$W_1 - W_2 > \begin{cases} 0.65 \,\mathrm{e}^{0.153 \,(W_2 - 13.86)^2} \,, & W_2 > 13.86 \,, \\ 0.65 \,, & W_2 \le 13.86 \,. \end{cases} \tag{4}$$

² https://doi.org/10.5281/zenodo.17087033

Table 3. Active Galactic Nucleus counts for each selection used in this paper.

AGN selection method	Reference	Description	No.
X-ray	RW25	Extragalactic point-like X-rays sources from 4XMM-DR13, CSC2, and eROSITA surveys	437
DESI, spectroscopy	Siudek et al. (2024)	Spectroscopic diagnostics based on emission lines for the matched DESI sources (see Sect. 3)	160
DL-based	MB25	Galaxies with a predicted $f_{PSF} > 0.2$, based on VIS images	23 338
C75, AllWISE	A18	75% Completeness-optimised MIR diagnostic Eq. (3) applied to the AllWISE data	5712
R90, AllWISE	A18	90% Reliability-optimised MIR diagnostic Eq. (4) applied to the AllWISE data	556

These criteria were accompanied by some extra conditions. We only considered sources with W_1 and W_2 magnitudes fainter than the saturation limits of the survey set as $W_1 > 8$ and $W_2 > 7$ (Vega magnitudes), with $S/N_{W_2} > 5$, and not flagged as either artefacts or affected by artefacts, meaning that the cc_flags are equal to zero (MZ25). In the case of EDF-F and EDF-S, multiple WISE fluxes are available, including the AllWISE and the LegacyDR10 WISE fluxes. The main difference is that the latter are obtained through forced photometry at the locations of the Legacy Surveys optical sources, resulting in a larger number of matches with *Euclid* counterparts. Moreover, the extra conditions of the A18 diagnostics are not easily applicable to the LegacyDR10 WISE data. Therefore, considering that the EDF-N has only AllWISE data, we decided to work with the AllWISE MIR data also for EDF-F and EDF-S.

Sources with an X-ray counterpart identified by RW25. Several X-ray surveys observed the EDFs, such as the XMM-Newton 4XMM-DR13 survey (Webb et al. 2020), the Chandra Source Catalogue v.2.0 (CSC2; Evans et al. 2024), and the eROSITA DR1 Main sample (Predehl et al. 2021; Merloni et al. 2024). RW25 identified Q1 counterparts from these Xray surveys using the Bayesian algorithm NWAY (Salvato et al. 2018). The final product is a catalogue of Q1 sources matched with several X-ray point-like sources. This catalogue also includes spectroscopic redshift, if available, otherwise photo-z, Xray luminosities (L_X) , and a galactic or extragalactic probability (Gal_proba). We refer the reader to RW25 for more details about the optical-X-ray matching procedure and the catalogue generation. To select a pure sample of X-ray AGN, we selected only sources with match_flag = 1, Gal_proba < 0.5, optical signal-to-noise $S/N \ge 2$, and $L_X \ge 10^{42}\,\mathrm{erg\,s^{-1}}$. This soft X-ray luminosity threshold is generally sufficient for isolating AGN from other X-ray sources (Aird et al. 2017).

The MZ25 multi-wavelength catalogue provided DESI spectroscopic counterparts for 42 706 galaxies, and thus allowed for spectroscopic AGN detection. We ran several diagnostics to identify quasars (QSOs) and AGN candidates based on these spectroscopic data. To select QSOs, we utilised the DESI spectral-type classification (SPECTYPE=QSO; DESI Collaboration et al. 2024). For sources classified as galaxies (SPECTYPE=GALAXY), we used several methods to identify AGN based on emission line fluxes, widths, and equivalent widths measured with FastSpecFit (Moustakas et al. 2023). MZ25 reports the details of these measurements, available for 40 274 of the DESI EDR Q1 sources. This sample was accompanied by SED fitting performed by Siudek et al. (2024), which provided stellar masses and AGN properties. They only kept sources with

an SED fit with a reduced $\chi^2 < 17$. With these criteria, we found 160 counterparts in our stellar-mass-limited sample. This threshold for χ^2 was adopted from Siudek et al. (2024), who, based on extensive visual inspections (their Appendix D.2), defined it as optimal for ensuring reliable SED fits in their value-added catalogue. For our DESI-selected AGN sample, the vast majority (139 out of 160) have even higher quality fits, with $\chi^2 < 5$, and excluding the remaining 21 sources with χ^2 between 5 and 17 does not qualitatively affect our results.

MB25 trained a DL-based algorithm to perform image decomposition in the VIS imaging data and provide an estimate of the PSF contribution (f_{PSF}) with respect to the total galaxy light in the observed flux. Following the same technique as in Margalef-Bentabol et al. (2024b), MB25 fine-tuned the pretrained DL-architecture Zoobot (Walmsley et al. 2023) to predict f_{PSF} from galaxy images. The training set consisted of mock Euclid observations of TNG galaxies, where central point sources were injected with randomly chosen f_{PSF} values in the range [0, 1). The resulting DL model achieves high accuracy and precision in recovering f_{PSF} , with a mean bias $\langle f_{PSF}[injected]$ $f_{PSF}[Zoobot]\rangle = -0.0078$, and a root mean square error of 0.051. Only about 5% of galaxies with $f_{PSF}[injected] < 0.05$ have a predicted $f_{PSF}[Zoobot] > 0.2$. Here, we labelled as DLbased AGN those galaxies with $f_{PSF} > 0.2$, which corresponds to a 4σ cut given the mean uncertainty in the $f_{\rm PSF}$ estimates, and ensures a high-purity sample. Although this f_{PSF} threshold aims for a high-purity selection of dominant central point sources, we acknowledge that the derived f_{PSF} may include contributions from nuclear star formation in addition to AGN, and that its completeness could be affected by heavy nuclear obscuration. A more detailed discussion of the method, its performance, validation, and comparison with traditional selection methods, is presented in Margalef-Bentabol et al. (2024b) and MB25. We also estimate the AGN luminosity in the VIS band (L_{PSF}) by multiplying the total galaxy flux by the predicted f_{PSF} and converting it into a luminosity using the photometric redshift.

In total, our sample includes 28 670 classified galaxies hosting an AGN identified by at least one of the selection methods above.³ The number of AGN identified per selection method is reported in Table 3. Many AGN have multiple detections. We show the intersection of the AGN selections in Appendix C. The MZ25 Q1 AGN catalogue includes a variety of AGN selections, among which an AGN identification diagnostic based on *Eu*-

³ Considering the whole sample, i.e. classified plus unclassified galaxies, about 39% of AGN are labelled as unclassified, similar to the non-AGN population, where the unclassified fraction is 36%.

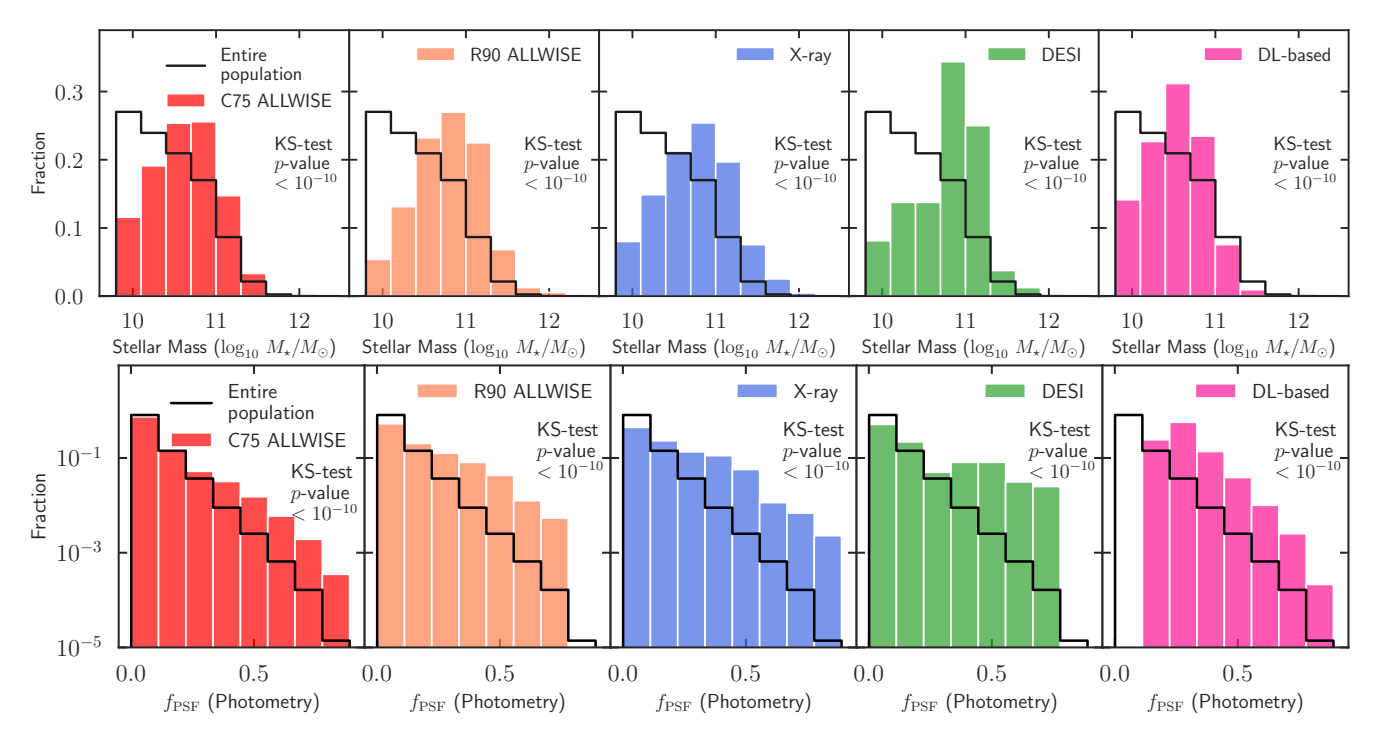


Fig. 5. Stellar mass (upper row) and point-source contribution, estimated by the PSF fraction (f_{PSF} , lower row) distributions for each AGN population. As a reference, we overlay the distribution for the entire sample of classified galaxies, including the selected AGN, in each panel. The distribution areas are normalised to unity. In each panel, we report the results of a two-sample KS test between the selected AGN and the entire galaxy sample.

clid's photometry alone (Euclid Collaboration: Bisigello et al. 2024). However, we did not consider this selection because its purity and completeness are poor in the absence of *u*-band observations. Moreover, this methodology is oriented towards obtaining a clean sample of quasars, which requires constraints on the point-like morphology of the source, which will bias against the detection of potential merging features.

For DESI- and X-ray-selected AGN, we computed the AGN bolometric luminosity. In the first case, we utilised the $L_{\rm bol}$ estimated through SED fitting by Siudek et al. (2024). The SED fitting was performed using Code Investigating GALaxy Emission (CIGALE v2022.1; Boquien et al. 2019; Yang et al. 2020, 2022), assuming for the AGN contribution the Fritz et al. (2006) templates. Siudek et al. (2024) found a close agreement between the $L_{\rm bol}$ derived from *Chandra* and SED fitting, with a median difference of $L_{\rm bol,SED}-L_{\rm bol,Chandra} \simeq -0.1$ dex. For the X-ray AGN, we used the X-ray luminosities ($L_{\rm X}$) from RW25, which we converted into bolometric luminosities using the conversion factors from Shen et al. (2020). Specifically, we used the double power law

$$\frac{L_{\text{bol}}}{L_{\text{X}}} = c_1 \left(\frac{L_{\text{bol}}}{10^{10} L_{\odot}} \right)^{k_1} + c_2 \left(\frac{L_{\text{bol}}}{10^{10} L_{\odot}} \right)^{k_2} , \tag{5}$$

where $c_1 = 5.712$, $k_1 = -0.026$, $c_2 = 12.60$, and $k_2 = 0.278$. We show how L_{bol} evolves with redshift for DESI and X-ray AGN in Fig. 4. X-ray sources are shown separately to highlight the difference in the survey characteristics (RW25). We note that 4XMM and CSC2 are deeper surveys compared to eROSITA, which covers a larger area but is biased towards brighter AGN ($L_{\text{bol}} \gtrsim 10^{45} \, \text{erg s}^{-1}$).

Different AGN selections correspond to different host galaxy properties (e.g., Silverman et al. 2008). We compare the stellar mass of the AGN candidates hosts for the different AGN selections in Fig. 5, top panels. Compared to the entire galaxy sample

(active and non-active galaxies), AGN candidates reside in more massive galaxies, with their M_{\star} distribution peaking at $10^{10.5}$ – $10^{11}\,M_{\odot}$. Nevertheless, we should bear in mind that the stellar masses derived by Euclid Collaboration: Enia et al. (2025) or the official *Euclid* pipeline do not consider the AGN component, which could bias the estimates of the M_{\star} of AGN host galaxies. For example, the Euclid Collaboration: Enia et al. (2025) M_{\star} are systematically lower by 0.07 dex compared to those derived for the DESI sample, which included an AGN component in their SED fitting (Siudek et al. 2024).

To assess the statistical difference among the AGN populations and the entire galaxy sample, we ran a two-sample Kolmogorov-Smirnov test (KS test; Hodges 1958). The KS test determines whether two samples come from the same parent distribution (null hypothesis). The p-value measures the probability of obtaining the observed difference between distributions, assuming the null hypothesis is true. If the p-value is below the significance level (here we take it to be 0.05), the difference between the two samples is statistically significant. In each panel of Fig. 5, we report the resulting p-value between each AGN selection and the entire galaxy sample. The results confirm that the M_{\star} distributions of AGN candidates are statistically different from the M_{\star} distribution of the entire sample (active plus non-active galaxies).

There are also some differences among the different AGN selections. DESI AGN live in extremely massive galaxies, with more than 70% of these galaxies having $M_{\star}/M_{\odot} \geq 10^{11}$. X-ray AGN and R90 MIR AGN tend to be in slightly less massive galaxies, with average $M_{\star}/M_{\odot} \simeq 10^{10.8}$, in agreement with previous studies (Bongiorno et al. 2012; Mountrichas et al. 2021). A KS test run to compare the M_{\star} distributions of AllWISE R90, X-ray, and DESI AGN with each other, confirms this similarity (p-value< 0.05). DL-based and C75 MIR AGN inhabit the least massive galaxies, with average $M_{\star}/M_{\odot} \simeq 10^{10.5}$. Also in this

case, we found agreement with previous studies in the literature (e.g., Bornancini et al. 2022). These differences might be due to selection biases. DESI AGN are spectroscopically selected and so naturally more likely to be in brighter, hence more massive, galaxies. Similarly, the difference between the stellar masses of R90 and C75 MIR AGN candidates hosts is expected because redder colours and brighter magnitudes are required (A18) to select more reliable samples of AGN. The DL algorithm used to identify AGN components was trained using galaxies down to $10^9 M_{\odot}$. Thus, it is not surprising that this method allowed us to select AGN in less massive galaxies than the other methods.

In Fig. 5, bottom panels, we compare the f_{PSF} distribution for the different AGN selections. As expected, all AGN types show a larger fraction of galaxies with higher f_{PSF} values compared to the entire galaxy sample. It is not surprising that the largest fraction of $f_{PSF} \ge 0.5$ galaxies is observed in DESI AGN, these being optically selected spectroscopic AGN. However, we might be missing the extremely dominant point sources ($f_{PSF} > 0.8$) because CIGALE fails to estimate the stellar mass correctly when the AGN outshines the host galaxy. The KS tests confirm the difference between AGN candidate hosts and the entire galaxy population. This statistical difference confirms that the f_{PSF} parameter effectively isolates galaxies with a prominent central luminous component, characteristic of AGN activity, across all selection methods. It also provides an additional validation for the statistical reliability of our DL-based method in quantifying the AGN contribution. In Appendix C, we also compared the redshift distributions of each AGN selection.

4. Results

In this section, we first construct control samples of mergers and non-mergers and AGN and non-AGN galaxies. Then, we investigate the merger and AGN relation by adopting a binary AGN-non-AGN classification and exploring continuous AGN parameters. All experiments are divided into two redshift bins, which are $0.5 \le z < 0.9$, and $0.9 \le z \le 2.0$, with roughly equal numbers of AGN.

4.1. Control pools

Proper control samples are crucial as AGN occurrence and the merger rate can depend on host galaxy properties such as stellar mass and redshift (e.g., Aird et al. 2012; Ferreira et al. 2020). Specifically, the merger and AGN control samples satisfy the following conditions:

$$|z_{\text{control}} - z_{\text{sample}}| \le 0.04 \ z_{\text{sample}},$$
 (6)

$$|\log_{10}(M_{\star,\text{control}}/M_{\star,\text{sample}})| \le 0.2 \,\text{dex} \,. \tag{7}$$

We chose these values according to the estimated normalised median absolute deviations for photo–z and M_{\star} (Euclid Collaboration: Enia et al. 2025). These two conditions ensure that each galaxy (AGN) is compared with a sample of galaxies with similar redshift and stellar mass. For each galaxy (AGN) in the original sample, we required at least ten counterparts that satisfy these criteria. When more than ten controls were found, we randomly picked ten of them. If there were fewer than ten controls, we iteratively increased our tolerances by a factor of 1.5 for each parameter. This operation was performed up to three times; otherwise, we rejected the galaxy (AGN). When constructing controls for AGN galaxies, we sampled from all galaxies that do not host any detected AGN, a pool of 330 931 possible galaxies. Non-AGN controls were constructed independently for each AGN selection.

While matching in other physical parameters, such as star formation rate, could further refine the control samples, we have not included these in the current analysis. Specifically, star formation rate estimates available in Q1 are subject to considerable uncertainties at this stage (e.g., normalised median absolute deviations of $\sim 0.45-0.64$ dex, as detailed in Euclid Collaboration: Enia et al. 2025). Given these large uncertainties, attempting to match the star formation rate would not improve the control.

Merger and AGN relation using a binary AGN classification

In the first set of experiments, we investigated whether mergers can trigger AGN by examining the incidence rate of AGN in mergers and non-merger controls, and whether they are the primary trigger, by comparing the merger fraction in AGN and non-AGN controls.

4.2.1. AGN frequency in mergers and non-mergers

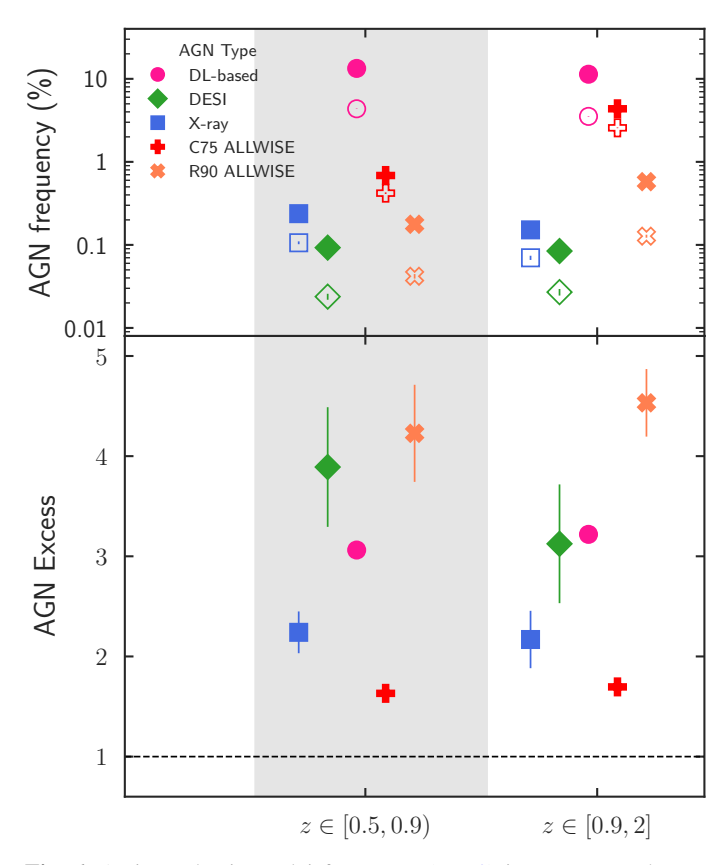


Fig. 6. Active galactic nuclei frequency (Eq. 8) in mergers and non-merger controls in two redshift bins. *Top*: Frequency of AGN in mergers (filled symbols) and non-merger controls (empty symbols). *Bottom*: AGN excess in mergers compared to non-merger controls. The excess is the AGN frequency in mergers divided by that in the relative non-mergers.

The frequency of AGN in mergers and respective non-merger controls, per AGN type, is reported in Table 4 and shown in Fig. 6. The frequencies and relative statistical uncertainties are estimated using bootstrapping with resampling (1000 samples for each population). In both classes, the AGN frequency is defined as the ratio of identified AGN in the merger class to the

Table 4. Frequency of selected AGN types in mergers and non-merger controls (Eq. 8), divided into two redshift bins.

AGN type	M	$0.5 \le z < 0.9$ NM (control)	Excess	M	$0.9 \le z \le 2.0$ NM (control)	Excess
X-ray RW25	$0.24 \pm 0.02\%$ (146/61 393)	$0.106 \pm 0.004\%$ (652/614411)	2.2 ± 0.2	$0.15 \pm 0.02\%$ (66/43 644)	$0.070 \pm 0.004\%$ (319/435 959)	2.2 ± 0.3
DESI Siudek et al. (2024)	$0.09 \pm 0.01\%$ (57/61 393)	$0.024 \pm 0.002\%$ (147/614411)	3.9 ± 0.6	$0.08 \pm 0.01\%$ (37/43 644)	$0.027 \pm 0.002\%$ (118/435 959)	3.1 ± 0.6
DL-based MB25	$13.3 \pm 0.1\%$ (8196/61 393)	$4.36 \pm 0.03\%$ (26 779/614 411)	3.06 ± 0.04	$ 11.4 \pm 0.1\% \\ (4960/43644) $	$3.52 \pm 0.03\%$ (15 387/435 959)	3.22 ± 0.05
C75 AllWISE A18	$0.69 \pm 0.03\%$ (420/61 393)	$0.420 \pm 0.008\%$ (2578/614411)	1.63 ± 0.09	$4.4 \pm 0.1\%$ (1902/43 644)	$2.57 \pm 0.02\%$ (11 195/435 959)	1.69 ± 0.04
R90 AllWISE A18	$0.18 \pm 0.02\%$ (109/61 393)	$0.042 \pm 0.003\%$ (258/614411)	4.2 ± 0.5	$0.58 \pm 0.04\%$ (252/43 644)	$0.127 \pm 0.005\%$ (555/435 959)	4.5 ± 0.3

Notes. M (NM) indicates mergers (non-mergers). Fractions and relative errors are calculated using bootstrapping with resampling (1000 samples for each population). In brackets, we provide the number of AGN for each type, over the total number of mergers and non-merger controls.

total number of objects in the merger class:

AGN frequency =
$$\frac{N_{\text{AGN}}}{N_{\text{all}}}$$
. (8)

For all AGN types, we observed a higher frequency of AGN in mergers than non-merger controls in both z bins, demonstrating that mergers are a viable method to fuel accretion onto SMBHs. To show it more clearly, we calculated the AGN excess, defined as the ratio of the AGN frequency in mergers relative to non-mergers. The AGN excess is reported in Table 4 and the lower panel of Fig. 6. X-ray AGN show the same excess (2.2) relative to controls in both redshift bins. Similarly, DL-based, MIR C75 and R90 AGN have consistent excess in both z bins, showing no clear signs of redshift evolution. On the contrary, DESI AGN go from an AGN excess of 3.9 at z < 0.9, to 3.1 at z > 0.9. However, this AGN selection shows larger uncertainties. Therefore, one must be cautious in inferring any redshift trends. Interestingly, the two MIR AGN selections exhibit completely different AGN excesses, with a much higher excess in the purer R90 selection. This could indicate that the C75 selection is highly contaminated by non-AGN galaxies. While these results indicate a clear excess of AGN activity in mergers, it is important to consider the potential impact of classification uncertainties inherent to automated methods, which we rigorously assess using detailed Monte Carlo (MC) simulations in Sect. 5.3.

Our results are in agreement with previous studies that adopted the same AGN excess definition. The optical AGN excess we observed is consistent with the 3.7 AGN excess reported by Bickley et al. (2023) for similar AGN in post-mergers, but it is much higher than the upper bound of 1.5 for the optical AGN excess found by Gao et al. (2020) (sample selections in both works, z < 0.3 and $M_{\star} > 10^9 M_{\odot}$). Regarding the X-ray AGN, the excess we found is comparable to the 1.8 excess found by Bickley et al. (2024, z < 0.3 and $M_{\star} > 10^8 M_{\odot}$), the 1.9 excess found by La Marca et al. (2024, at 0.5 < z < 0.8 and $M_{\star} > 10^9 M_{\odot}$), and the 2.2 excess reported by Lackner et al. (2014, 0.5 < z < 1 and $M_{\star} > 10^8 \, M_{\odot}$). Nevertheless, La Marca et al. (2024) observed a much lower X-ray AGN excess of 1.3 at z < 0.5, while Secrest et al. (2020) found no statistically significant evidence for an Xray AGN excess in post-mergers at z < 0.2 and $M_{\star} > 10^{9.5} M_{\odot}$. However, the latter work showed a much larger excess for MIRselected AGN, suggesting that AGN in post-mergers are more likely to be heavily obscured. In fact, several other studies reported a larger excess of MIR AGN in mergers compared to nonmerger controls, reaching a factor of 3-7 (Goulding et al. 2018; Bickley et al. 2023; La Marca et al. 2024), which is in agreement with our results of the more reliable MIR AGN selection (R90).

Our results and previous studies allow for some robust conclusions and some speculation. These findings robustly imply that major mergers trigger and fuel AGN, independently of AGN selection and the redshift. Considering that the purest MIR AGN show a larger excess than other AGN selections, we could speculate that mergers are more strongly connected to the triggering of dust-obscured AGN. For example, a major merger could redistribute gas and dust within a galaxy, increasing the dust obscuration surrounding the central active nucleus. This obscuration, if particularly heavy, might also make the detection of optical and soft X-ray AGN more challenging, partially explaining the lower excesses for these AGN.

4.2.2. Merger fraction in AGN and non-AGN

Table 5 and Fig. 7 report the merger fraction (f_{merg} , Eq. 2) in AGN and corresponding non-AGN controls, divided by AGN type. In both z bins, and for each AGN type, the fraction of mergers is higher for AGN than for non-AGN controls, reinforcing the merger-AGN connection. All AGN types, excluding the Xray-selected ones, do not show signs of redshift evolution for the f_{merg} in AGN and non-AGN. The difference in f_{merg} for X-ray AGN at z < 0.9 and $z \ge 0.9$ is within 2σ uncertainty. Across the entire redshift range, X-ray, DESI, DL-based, and R90 MIR AGN predominantly inhabit merging galaxies, with f_{merg} ranging from 44% to 65%. Only in the case of C75 MIR AGN, we reported a merger fraction of 40%, which might indicate a possibly higher contamination degree in this selection. On the other hand, non-AGN controls are classified as mergers in 25-28% of the cases, about a factor of two less frequently than for the AGN host galaxies. To confirm that these findings are not an artefact of imperfections in the merger classification process, we evaluate the influence of classification uncertainties on these merger fractions through the MC analysis detailed in Sect. 5.3.

Low-redshift studies have found that the fraction of mergers in the MIR-selected AGN is a factor of 1.5–2.3 larger than that of non-AGN controls, in agreement with our results (z < 0.8 and $M_{\star} > 10^9 M_{\odot}$; Ellison et al. 2019; Gao et al. 2020; La Marca et al. 2024). Likewise, Donley et al. (2018) found that IR-only AGN out to z = 5 are more likely to be classified as irregular, asymmetric, or interacting than as regular galaxies. For optically selected AGN, Ellison et al. (2019) found a merger fraction in AGN twice as large as that in non-AGN, similar to what we ob-

Table 5. Merger fraction (f_{merg}) in active galaxies (AGN) and non-active galaxies (non-AGN controls) for different AGN selections divided into two redshift bins.

	$0.5 \le z < 0.9$		$0.9 \le z \le 2.0$		
AGN type	$f_{\rm merg}({\rm AGN})$	$f_{\text{merg}}(\text{non-AGN controls})$	$f_{\rm merg}({\rm AGN})$	$f_{\text{merg}}(\text{non-AGN controls})$	
X-ray RW25	$51 \pm 3\%$ (146/288)	$24.7 \pm 0.8\% $ (726/2935)	$44 \pm 4\%$ (66/149)	$27 \pm 1\%$ (386/1435)	
DESI Siudek et al. (2024)	$59 \pm 5\%$ (57/97)	$26 \pm 1\%$ (257/982)	$59 \pm 6\%$ (37/63)	$26 \pm 2\%$ (161/618)	
DL-based MB25	$57.3 \pm 0.4\%$ (8196/14313)	$27.9 \pm 0.1\%$ (39 886/143 223)	$54.9 \pm 0.5\%$ (4906/9025)	$26.4 \pm 0.1\%$ (23 777/90 157)	
C75 AllWISE A18	$40 \pm 2\%$ (420/1041)	$27.4 \pm 0.4\%$ (2848/10404)	$40.7 \pm 0.7\%$ (1902/4671)	$26.9 \pm 0.2\%$ (12558/46716)	
R90 AllWISE A18	64 ± 4% (109/170)	$27 \pm 1\%$ (454/1705)	$65 \pm 2\%$ (252/386)	$27.3 \pm 0.7\% (1052/3855)$	

Notes. Fractions and relative errors are calculated using bootstrapping with resampling (1000 samples for each population). The numbers of AGN for each type, relative to the total number of mergers and non-merger controls in each *z*-bin, are provided in brackets.

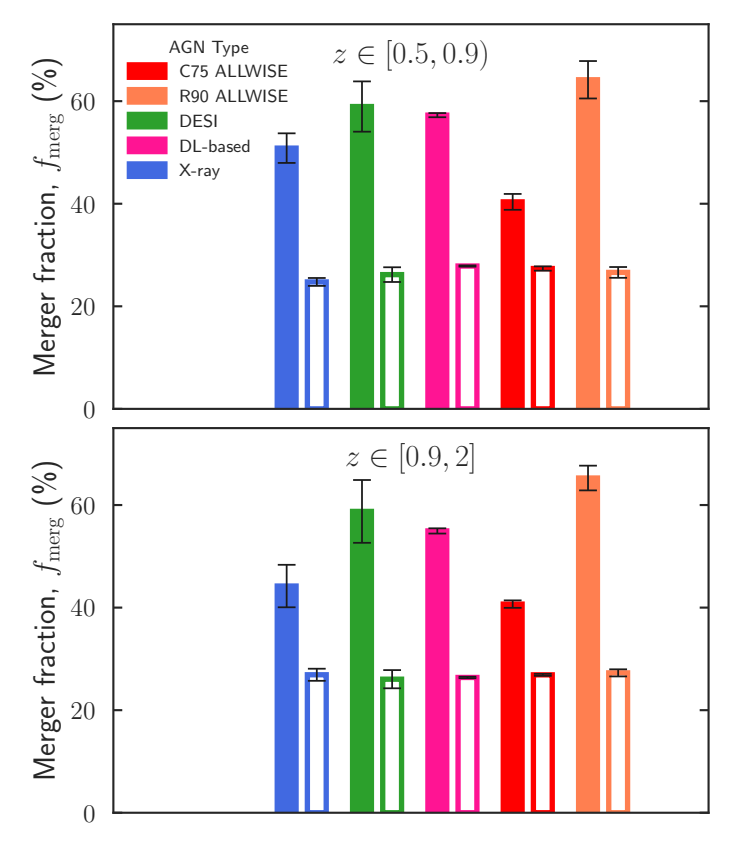


Fig. 7. Merger fraction for all AGN types (filled bars) and relative non-AGN controls (empty bars), divided into two redshift bins. The fraction of mergers is higher in the AGN samples than in the non-AGN controls for all AGN types in both bins.

serve for the DESI AGN. In contrast, Gao et al. (2020) reported an excess of $f_{\rm merg}$ in optical AGN of a factor below 1.5. For X-ray-selected AGN, Bickley et al. (2024) reported an $f_{\rm merg}$ excess of a factor of 2, while La Marca et al. (2024) found an excess of 1.3 at $z \le 0.5$ and of 1.8 at 0.5 < z < 0.8, close to our findings. At higher redshift ($1 \le z \le 2$), other studies uncovered only a marginally higher fraction of mergers in X-ray AGN compared to non-AGN, comparable with no excess at all ($M_{\star} \gtrsim 10^{9.5} M_{\odot}$; Cisternas et al. 2011; Kocevski et al. 2012; Marian et al. 2019), although these samples are limited to intermediate AGN luminosity (X-ray luminosity $10^{42} < L_{\rm X} < 10^{44} {\rm erg \, s^{-1}}$). Recently,

Villforth (2023) reviewed several studies in the literature about the merger fraction in AGN and non-AGN controls. They concluded that f_{merg} in X-ray-selected AGN are consistent with no excess over controls, in contrast with our findings, while for optically selected AGN, there is an excess over control samples, in agreement with our results for DESI AGN.

Although the elevated merger fractions observed in AGN hosts point to a connection between mergers and nuclear activity, caution is needed when interpreting the role of mergers as a primary triggering mechanism. First, a non-negligible merger fraction (25–28%) is also observed in the non-AGN control samples. Second, our analysis is limited to classified galaxies and does not include sources below our detection and classification thresholds, which may introduce biases and incompleteness. Therefore, our results do not allow us to quantify the exact contribution of mergers relative to other triggering channels.

4.3. The merger and AGN connection using continuous parameters

In this second set of experiments, we examined the merger-AGN connection using continuous parameters, which characterise either the relative or the absolute AGN power. Specifically, we first analysed the PSF fraction, $f_{\rm PSF}$, which assesses the power of an AGN relative to its host galaxy. Then, we concentrated on the AGN luminosity for studying the absolute AGN power.

4.3.1. Dependence on the relative AGN power

Here we analysed the connection between mergers and the PSF fraction parameter, $f_{\rm PSF}$, which measures the relative nuclear power. We reported the $f_{\rm PSF}$ normalised distributions for mergers and relative non-merger control galaxies in Fig. 8. Mergers show a larger fraction of galaxies in the range $0.1 \leq f_{\rm PSF} < 0.8$ than non-merger controls, in both redshift bins. The only exception is represented by the $f_{\rm PSF} > 0.8$ galaxies at $z \geq 0.9$. We show the results of KS tests in each panel of Fig. 8. The KS test output strongly excludes the null hypothesis, that is, the difference between the $f_{\rm PSF}$ distribution for mergers and non-merger controls is statistically significant, in both z bins. This hints towards a scenario where mergers fuel the accretion onto the SMBH, enhancing its accretion rate and, consequently, the point-source luminosity and contribution to the total galaxy light.

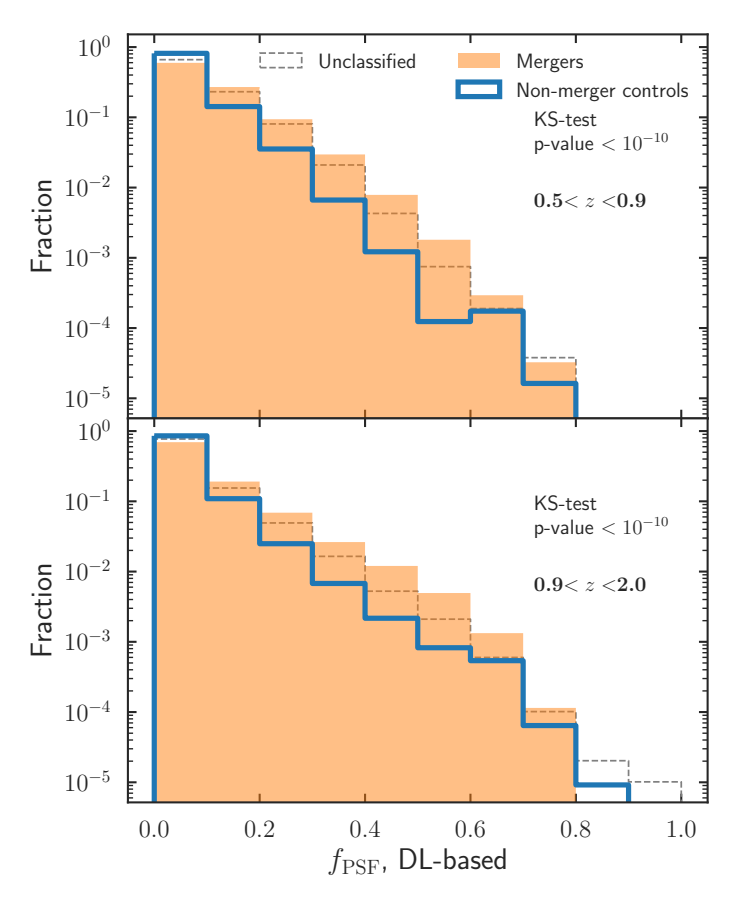


Fig. 8. Normalised distributions of the PSF fraction for mergers and non-mergers, in the two redshift bins. The results of a two-sample KS test are reported in each panel. The $f_{\rm PSF}$ -normalised distribution for unclassified galaxies is overlaid as a comparison.

We present the merger fraction versus f_{PSF} relationship for all galaxies in Fig. 9, divided into redshift bins. We calculated the merger fraction in N f_{PSF} bins, logarithmically spaced in the range 0–0.86 (the maximum f_{PSF} in our sample). The number

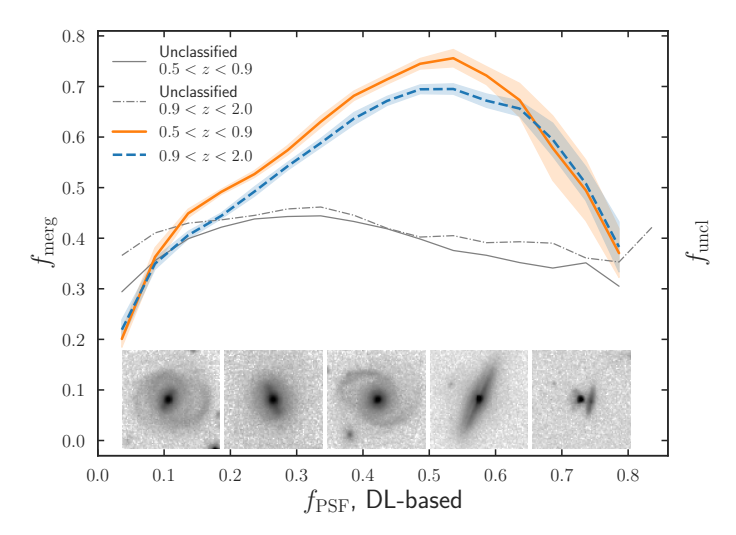


Fig. 9. Merger fraction and PSF contribution fraction relationship for the two redshift bins considered. All AGN are included. Trend lines represent the running median, while the shaded areas are one standard deviation. Examples of *Euclid* images of galaxies with increasing levels of $f_{\rm PSF}$ are shown at the bottom. Cutouts are $8'' \times 8''$, log-scaled in the 1st–99th percentile range. Grey lines indicate the fraction of unclassified objects as a function of $f_{\rm PSF}$.

of bins N is randomly sampled between 6 and 20. Bootstrapping with resampling is used (1000 samples for each population). The trends reported represent the running median of all outcomes and the respective 1σ uncertainties, for each population. A clear trend emerges for both redshift bins. From $f_{\rm PSF}=0$ up to $f_{\rm PSF}=0.55$, the fraction of mergers monotonically increases, from $f_{\rm merg}=0.2$ to $f_{\rm merg}\simeq0.7$. After this peak value, the merger fraction declines with increasing $f_{\rm PSF}$, down to $f_{\rm merg}=0.4$ at $f_{\rm PSF}=0.8$. Uncertainties become larger with increasing $f_{\rm PSF}$, mostly due to fewer galaxies in those bins. In the range $0.2 \le f_{\rm PSF} \le 0.75$ mergers appear to be the dominant mechanism to trigger AGN ($f_{\rm merg}>0.5$).

The trend inversion for $f_{PSF} = 0.55$, where f_{merg} begins to decline despite increasing PSF dominance, presents a complex interpretive challenge. We specifically investigated if this decline is primarily due to the dominant PSF outshining the host galaxy's morphological features, thereby making merger identification more difficult. To test this, we performed an experiment using a randomly selected sample of ~ 1500 galaxies without an injected PSF from our test set. Focusing on the dominant regime ($f_{PSF} > 0.55$), we re-classified simulated galaxies after injecting a prominent PSF component into the host galaxies from this sample. Our analysis revealed that only approximately 4% of simulated galaxies originally classified as mergers were relabelled as non-mergers or unclassified after a dominant PSF was added. This indicates that while a dominant PSF can marginally hinder morphological classification, it is not the primary driver for the observed steep decline in f_{merg} at the highest f_{PSF} values. An alternative explanation might lie in the fact that f_{PSF} is a relative quantity. Although extremely dominant, a point source could be faint in absolute terms, in which case mergers might play a minor role, as we show in the next section.

To investigate possible differences among the various AGN selections, we analysed in Appendix D the $f_{\rm merg}$ versus $f_{\rm PSF}$ relation for individual AGN types. The C75 MIR AGN show a trend similar to the whole galaxy population, while the trend is less clear in the case of the DESI and X-ray AGN, probably due to the lower number statistics. R90 MIR AGN have a very high $f_{\rm merg}$ (> 60%) for the whole $f_{\rm PSF}$ range.

In La Marca et al. (2024), the authors estimated the relative AGN power, the AGN fraction parameter (f_{AGN}), through SED fitting. This f_{AGN} is the fraction of light emitted by the AGN component over the total galaxy light, in the wavelength range 3–30 µm. This particular wavelength range was chosen as it robustly probes the re-emission from warm dust in the AGN torus, making it a reliable indicator of AGN activity, particularly for obscured sources (Hickox & Alexander 2018). They presented an f_{merg} versus f_{AGN} relation with two regimes, for all AGN types considered: f_{merg} is rather flat as a function of f_{AGN} for relatively subdominant AGN, then it steeply rises above 50% for the most dominant AGN ($f_{AGN} \ge 0.8$). Although we estimated the AGN relative contribution through photometry, there are some similarities. First, for less dominant AGN ($f_{PSF} \le 0.2$), mergers are not the main AGN triggering mechanism. Second, major mergers are the principal pathway to fuel more dominant AGN. Yet, some differences exist. The f_{merg} versus f_{PSF} relation does not show any flat regime, but rather $f_{\rm merg}$ constantly increases, and subsequentially decreases, as a function of f_{PSF} . Overall, these results support the idea that mergers can enhance AGN fuelling and are the prevailing mechanism for producing dominant AGN with respect to their host galaxy. In contrast, less dominant AGN may be primarily fuelled by other mechanisms, such as secular processes (e.g., Cisternas et al. 2011; Schawinski et al. 2011; Treister et al. 2012).

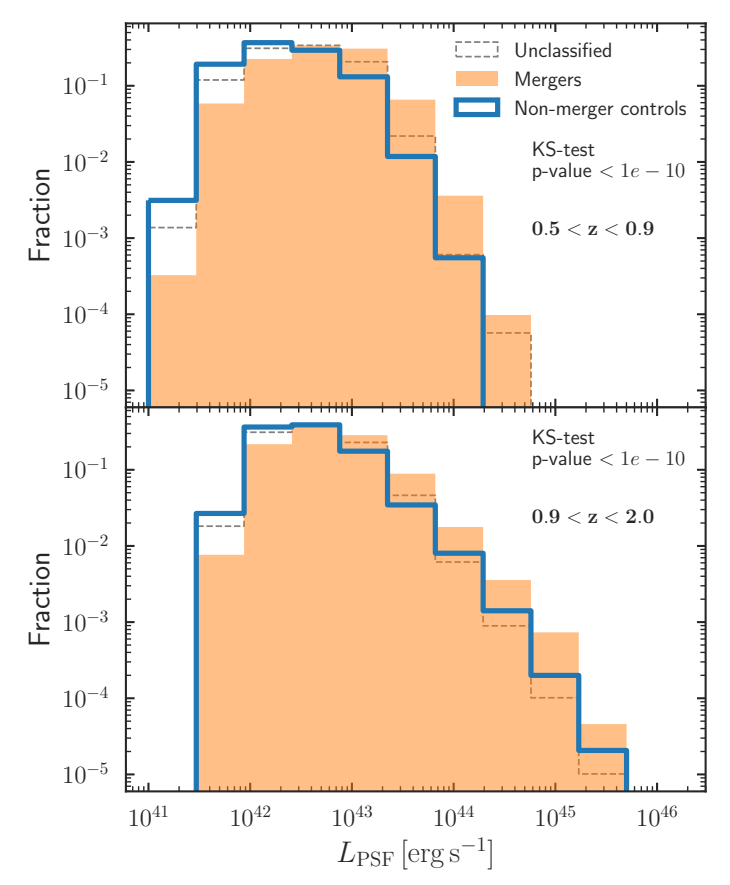


Fig. 10. Normalised distributions of the PSF luminosity for mergers and non-mergers, in the two redshift bins. The results of a two-sample KS test are reported in each panel. The $f_{\rm PSF}$ -normalised distribution for unclassified galaxies is overlaid as a comparison.

4.3.2. Dependence on the absolute AGN power

Next, we analysed the AGN luminosity parameters, which trace the absolute AGN power. Specifically, we focused on the point source luminosity, $L_{\rm PSF}$, and the bolometric luminosity, $L_{\rm bol}$, where the latter is available only for the X-ray and DESI AGN (see Sect. 3 for details on the derivation of $L_{\rm bol}$).

We present the normalised distributions of L_{PSF} for mergers and non-merger controls in Fig. 10. In both redshift bins, we observed a higher fraction of mergers at $L_{PSF} > 10^{43} \,\mathrm{erg \, s^{-1}}$ compared to non-merger controls. Therefore, mergers are more likely to harbour a bright AGN than the relative non-merger control galaxies. We show the normalised L_{bol} distribution for mergers and non-merger controls in Fig. 11. In the case of the X-ray AGN, mergers and non-mergers have similar L_{bol} distributions, with some differences at the very bright end in both z bins. Indeed, a larger fraction of mergers host a bright AGN ($L_{\rm bol} \geq 10^{46}\,{\rm erg\,s^{-1}}$) compared to non-mergers. The KS test confirms such a difference in both z bins. In the case of the DESI AGN, this difference emerges at lower luminosities, at $L_{\rm bol} \ge 10^{45}\,{\rm erg\,s^{-1}}$ for the $0.5 \le z < 0.9$ bin, and at $L_{\rm bol} \ge 10^{44}\,{\rm erg\,s^{-1}}$ for the $0.9 \le z \le 2.0$ bin. For both X-ray and DESI AGN, in both redshift bins, the brightest AGN seem to inhabit almost exclusively interacting galaxies, hinting towards a picture where major mergers are responsible for fuelling the most powerful AGN. We evaluated the significance of this overabundance by performing a two-proportion z-test, comparing the fraction of bright X-ray ($L_{bol} > 5 \times 10^{45} \, \mathrm{erg \, s^{-1}}$) and DESI ($L_{bol} > 10^{45} \, \mathrm{erg \, s^{-1}}$) AGN in mergers and non-merger controls, in both redshift bins. The

results showed that these differences are statistically significant (p-value< 0.05) in all cases, except for the DESI AGN in the $0.9 \le z \le 2.0$ bin (p-value= 0.43).

We plot the merger fraction as a function of $L_{\rm PSF}$ in Fig. 12, using the same methodology as for the $f_{\rm PSF}$ - $f_{\rm merg}$ relation. For both redshift bins, $f_{\rm merg}$ increases as a function $L_{\rm PSF}$. At z < 0.9, $f_{\rm merg}$ show a steeper monotonic rise, with most of the galaxies being in mergers at $L_{\rm PSF} \simeq 10^{43.5}~{\rm erg\,s^{-1}}$. This happens towards higher luminosities at $0.9 \le z \le 2.0$, when we observe a flat $f_{\rm merg}$ in the range 10^{43} -5 × $10^{44}~{\rm erg\,s^{-1}}$, and mergers become prevalent only for the very bright end of the AGN population, $L_{\rm PSF} > 10^{45}~{\rm erg\,s^{-1}}$. This might indicate that at higher redshift, when larger gas supplies are available within galaxies (Tacconi et al. 2010), major mergers are less important in fuelling bright AGN. At the same time, at z < 0.9, when less gas is available, mergers might be the sole viable path to fuel such powerful AGN. We perform the same analysis but for individual AGN selections in Appendix D.2.

To quantify the statistical significance of these apparent redshift differences in the f_{merg} versus L_{PSF} relation, we performed two-proportion z-tests comparing the merger fractions in four equally spaced L_{PSF} bins spanning the range 10^{42} to 10^{44} erg s⁻¹, where the data from both redshift samples overlap. In all four luminosity bins tested, we find that the merger fraction in the lower redshift bin $(0.5 \le z < 0.9)$ is significantly higher than in the higher redshift bin $(0.9 \le z \le 2.0)$, with p-values < 0.001. This statistically confirms the visual impression from Fig. 12 that, at a given L_{PSF} , mergers are more prevalent at lower redshifts in our sample. However, it is important to note that when the uncertainties arising from the merger classification process are considered (as detailed in our MC simulations in Sect. 5.3), the shaded error regions for the two redshift trends show considerable overlap. This suggests that the true underlying difference might be less pronounced once the full impact of potential misclassifications is taken into account.

Finally, we present the merger fraction versus AGN bolometric luminosity relationship for DESI and X-ray AGN, and previous literature results (Urrutia et al. 2008; Treister et al. 2012; Glikman et al. 2015), in Fig. 13. As for the $f_{\rm merg}$ and $f_{\rm PSF}$ relation, we calculated the $f_{\rm merg}$ in N $L_{\rm bol}$ -bins, randomly sampled in the range 10^{42} – 10^{47} erg s⁻¹. Bootstrapping with resampling was used to estimate uncertainties. In both cases, given that there are only a few numbers in each bin, we report large uncertainties, of the order $f_{\rm merg} = 0.1 - 0.15$. These large uncertainties do not allow for strong conclusions to be drawn. X-ray AGN show a clear trend: the fraction of mergers increases with increasing luminosity. DESI AGN show a less clear trend, having an initially $(L_{\rm bol} \leq 10^{45}~{\rm erg~s^{-1}})$ decreasing merger fraction followed by a steady increase with increasing $L_{\rm bol}$. In both cases, major mergers appear as the dominant triggering mechanism of the most luminous AGN.

Our finding that the $f_{\rm merg}$ increases with bolometric AGN luminosity, particularly for the X-ray AGN sample, and that $f_{\rm merg}$ is particularly high for the most luminous AGN ($L_{\rm bol} \gtrsim 10^{45.5}~{\rm erg~s^{-1}}$) is consistent with previous work. For instance, Urrutia et al. (2008) and Glikman et al. (2015) found very high merger fractions, $f_{\rm merg} > 80\%$, for luminous, dust-reddened quasars. Similarly, Treister et al. (2012) found similar results and argued that major mergers are essential for fuelling the most luminous AGN. While direct comparison of absolute merger fractions is challenging due to different merger identification techniques, AGN selection methods, and redshift ranges, the qualitative trend of mergers playing an increasingly dominant role at

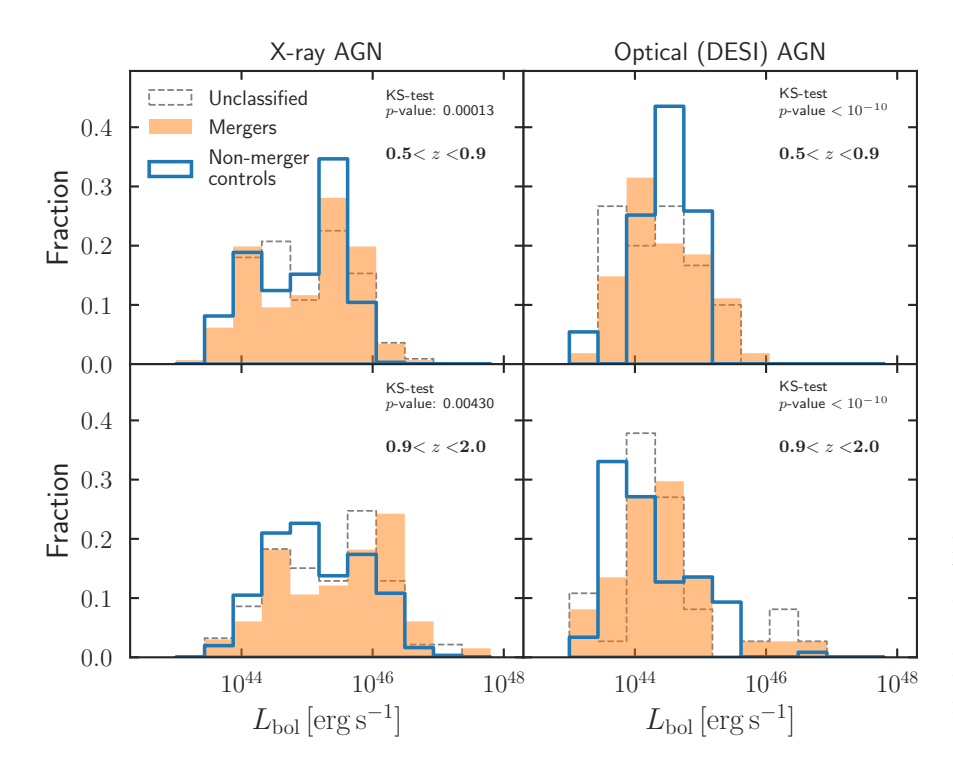
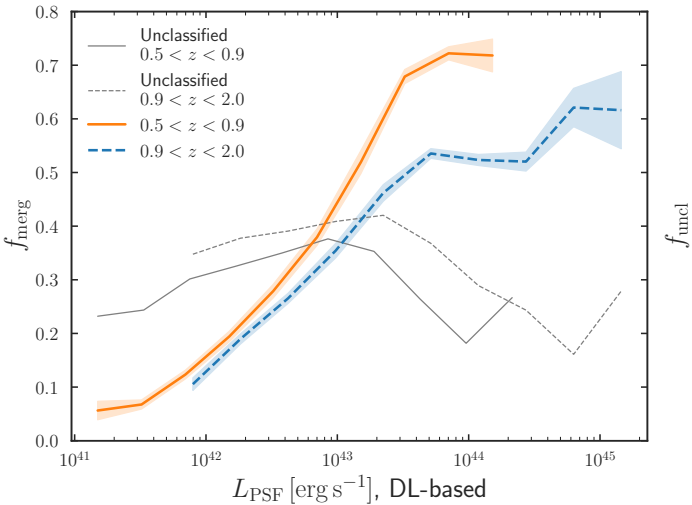
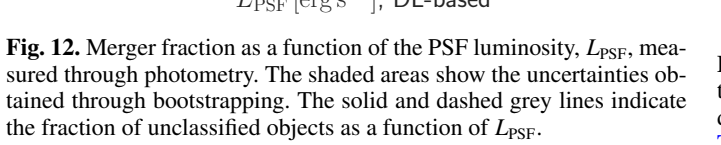


Fig. 11. Normalised distributions of the AGN bolometric luminosity for mergers and non-merger controls in the two redshift bins for the X-ray AGN (*left* column) and the DESI-selected AGN (*right* column). We report the results of a two-sample KS test in each panel. The $f_{\rm PSF}$ normalised distribution for unclassified galaxies is overlaid as a comparison





higher AGN luminosities is a common theme (see also Donley et al. 2018; Ellison et al. 2019; La Marca et al. 2024). For producing such powerful emissions, a large amount of matter must be fed to the central SMBH, and major mergers are an efficient way of bringing large amounts of gas to the centres of galaxies (Blumenthal & Barnes 2018).

5. Caveats discussion

In this section, we investigate the main factors that might influence the relationship between mergers and the AGN properties characterised by the continuous parameters $f_{\rm PSF}$ and $L_{\rm PSF}$, potentially affecting our results and conclusions. We discuss the role of unclassified galaxies, the dependency on stellar mass, and the systematics in our classification.

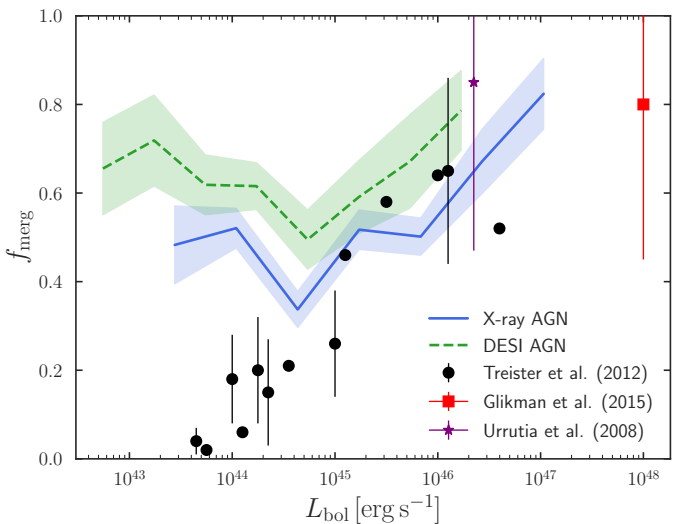


Fig. 13. Merger fraction and bolometric AGN luminosity relation for the X-ray and DESI-selected AGN. Trend lines show the running median, and shaded areas are one standard deviation. We include data from Treister et al. (2012, black circles), Urrutia et al. (2008, purple star), and Glikman et al. (2015, red square), with the associated $f_{\rm merg}$ uncertainties, if available.

5.1. The unclassified galaxies

First, we examined the impact of the unclassified galaxies on the observed trends. Figure 8 presents the normalised $f_{\rm PSF}$ distributions for the unclassified galaxies, which lie between the distributions of the non-merger controls and the mergers. This intermediate positioning likely reflects their mixed composition. However, mergers remain dominant over unclassified galaxies, with significantly higher fractions in the range $f_{\rm PSF}=0.1-0.8$. To test whether unclassified galaxies influence the observed $f_{\rm merg}$ - $f_{\rm PSF}$ trends, we analysed how the fraction of unclassified galaxies ($f_{\rm uncl}$) varies with $f_{\rm PSF}$. The results, shown in Fig. 9, indicate that $f_{\rm uncl}$ remains roughly constant in both redshift bins,

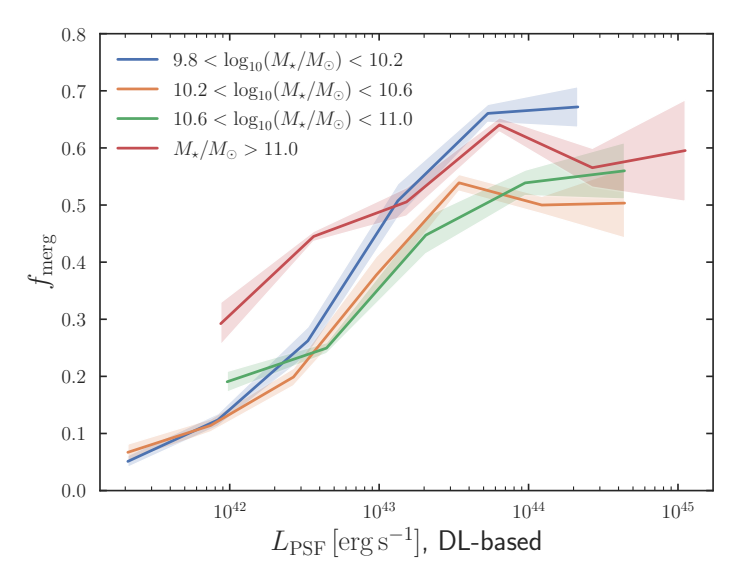


Fig. 14. Similar to Fig. 12 but with the merger fraction and PSF luminosity relation divided in stellar mass bins.

varying very mildly within the range $f_{\rm uncl} = 0.3$ –0.4. These findings suggest that unclassified objects do not significantly impact the relationship between major mergers and $f_{\rm PSF}$. Indeed, this result strengthens our overall conclusion that mergers are predominantly associated with relatively bright central point sources, serving as the primary mechanism for fuelling dominant AGN.

We also investigated the role of unclassified galaxies in the mergers and AGN luminosity relation. Figures 10 and 11 overlay the normalised $L_{\rm PSF}$ and $L_{\rm bol}$ distributions for unclassified sources. These comparisons indicate that major mergers primarily trigger the most luminous AGN, since they exhibit a significant excess compared to both non-merger controls and unclassified galaxies. Furthermore, we computed $f_{\rm uncl}$ as a function of $L_{\rm PSF}$ for both redshift bins (Fig. 12). The fraction remains relatively stable at 0.25–0.35 up to $L_{\rm PSF}=10^{43}~{\rm erg~s^{-1}}$, before decreasing to 0.2 for brighter AGN. These marginal variations do not alter the main finding that mergers play an increasingly significant role in fuelling the most luminous AGN.

5.2. The effect of stellar mass

Another potential concern is whether brighter, and consequently more massive, galaxies are more likely to be classified as mergers. To assess whether the observed trends primarily arise from the galaxy stellar mass, we examined the $f_{\rm merg}$ - $L_{\rm PSF}$ relation in four stellar mass bins, each containing a similar number of galaxies. The results (Fig. 14) confirm the general trend observed in Fig. 12: the merger fraction increases with $L_{\rm PSF}$ and then flattens for the most luminous point sources ($L_{\rm PSF} > 10^{43.5} {\rm erg \ s^{-1}}$), where mergers constitute the majority of the population. The most massive galaxies ($M_{\star} > 10^{11} M_{\odot}$) exhibit the highest $f_{\rm merg}$ on average, consistent with recent studies reporting a positive correlation between $f_{\rm merg}$ and stellar mass (e.g., Nevin et al. 2023). Thus, we conclude that stellar mass is not the primary driver of the $f_{\rm merg}$ - $L_{\rm PSF}$ relation.

5.3. Systematics in the classification

A key aspect of this study relies on the automated classification of galaxies into mergers and non-mergers using a CNN. As detailed in Sect. 3.1 and Table 2, our classifier achieves performance levels comparable to contemporary studies, with a precision of 0.80 and recall of 0.68 for the merger class, and a precision of 0.72 and recall of 0.83 for the non-merger class. While these metrics are robust, they inevitably imply that our classified samples contain non-negligible fractions of misclassified objects and are incomplete. Throughout our manuscript, we relied on statistical uncertainties under the assumption that our classifier perfectly distinguishes mergers from non-mergers. It is therefore crucial to assess the impact of these classification uncertainties on our main scientific findings, derived from both the binary comparisons (Sect. 4.2) and the analysis of continuous AGN properties (Sect. 4.3).

To quantitatively evaluate the robustness of our results against these misclassifications, we performed a detailed MC simulation based directly on the classifier's performance metrics. ⁴ The core simulation procedure involved 1000 independent iterations. In each iteration, we did the following:

- 1. We simulated the effect of contamination (finite precision). Based on the measured precision for mergers ($p_{\text{merger}} = 0.80$), a fraction ($1 p_{\text{merger}} = 20\%$) of galaxies initially classified by our CNN as mergers were randomly selected and temporarily relabelled as non-mergers. Similarly, based on the precision for non-mergers ($p_{\text{non-merger}} = 0.72$), a fraction ($1 p_{\text{non-merger}} = 28\%$) of galaxies initially classified as non-mergers were randomly selected and temporarily assigned to the merger class. This step yielded temporary 'corrected' classifications for all galaxies within that iteration.
- 2. We accounted for the classifier's incompleteness (finite recall). To estimate fractions relative to the total underlying population in any given subsample (e.g., AGN hosts, specific luminosity bins), rather than just the classified population, we applied weights based on the recall values. Any galaxy temporarily labelled as 'merger' in the iteration received a weight $w_{\rm M} = 1/{\rm recall_M} = 1/0.68$. Any galaxy labelled as 'non-merger' received a weight $w_{\rm NM} = 1/{\rm recall_{NM}} = 1/0.83$. This weighting statistically corrects the counts for the classifier's detection efficiency.

Using these temporary weighted classifications from each MC iteration, we recalculated our key metrics presented in Tables 4 and 5 and recomputed the f_{merg} - L_{PSF} relation (Fig. 12).

5.3.1. Systematic uncertainties on the binary experiments

For each MC iteration, we recalculated the AGN frequency in mergers and non-mergers presented in Table 4, for each AGN type and in both redshift bins, using the relabelled outcomes. The ratio of the two frequencies above was calculated for each iteration, producing a distribution for the AGN excess. The results of these simulations confirm the robustness of our binary analysis findings. Across the 1000 MC iterations, the AGN frequency was consistently found to be higher in the simulated merger populations compared to the non-merger controls for all AGN types and redshift bins considered. We plot in Fig. 15 the median AGN excess derived from the 1000 iterations, alongside the 2.5th to 97.5th percentile for each AGN type and redshift bin. This range represents the central 95% interval of the simulated outcomes,

⁴ Quantitatively assessing and propagating classification systematics (contamination and incompleteness) has historically been challenging in merger studies, due to the absence of precise performance metrics. Our detailed MC simulation represents a significant step forward in rigorously assessing the impact of classification uncertainties on large statistical samples.

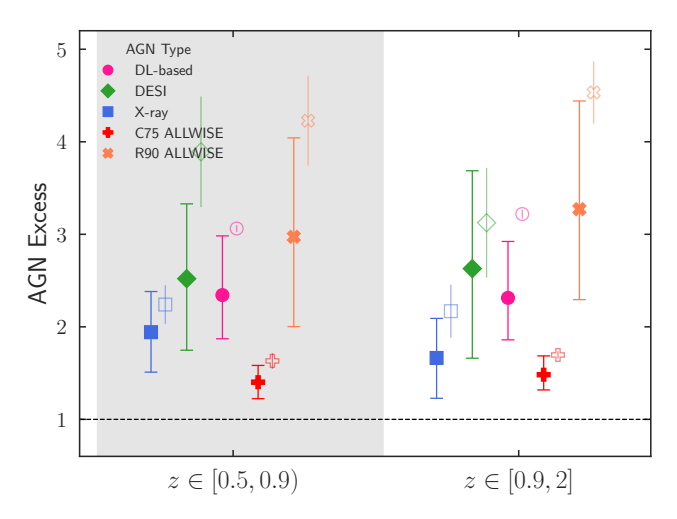


Fig. 15. Monte Carlo simulation outcomes for the AGN excess in mergers compared to non-merger controls. The symbols represent the median value of each AGN excess distribution, while the error bars cover the 2.5th-97.5th percentile range. Empty, transparent symbols represent the results presented in Fig. 6.

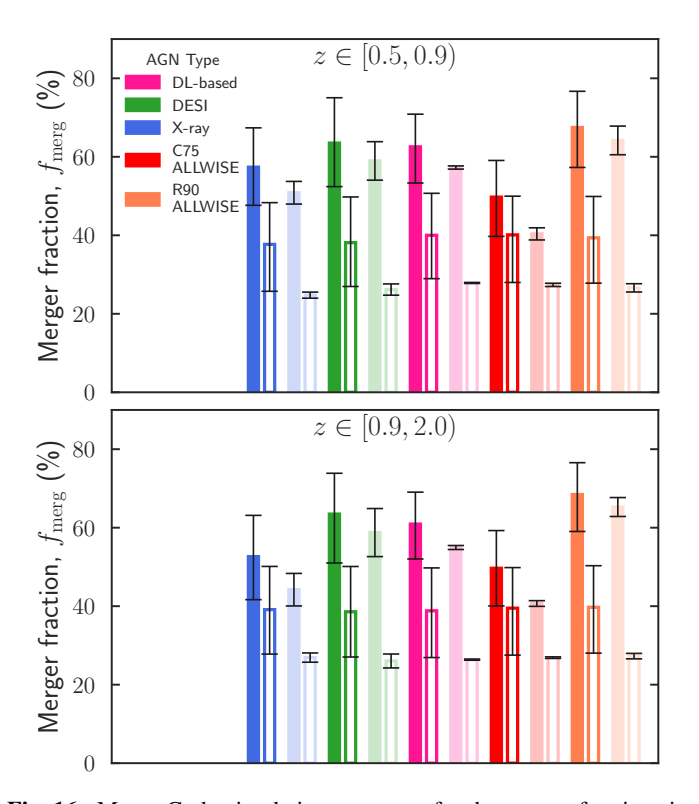


Fig. 16. Monte Carlo simulation outcomes for the merger fractions in AGN and non-AGN control sample (empty bars). The bars show the median value of the 1000 MC simulations, while the error bars display the 2.5th-97.5th percentile range. Results from Fig. 7 are reported as transparent bars.

effectively illustrating the statistically dominant parameter space explored when accounting for potential misclassifications. The median values are generally lower than the corresponding AGN excesses presented in Fig. 6, but still within the parameter space covered. As evident in Fig. 15, even considering the full extent of these uncertainties, the lower bound of the simulated AGN excess consistently remains well above unity, confirming that the observed excess is statistically significant and not merely an artefact of misclassification.

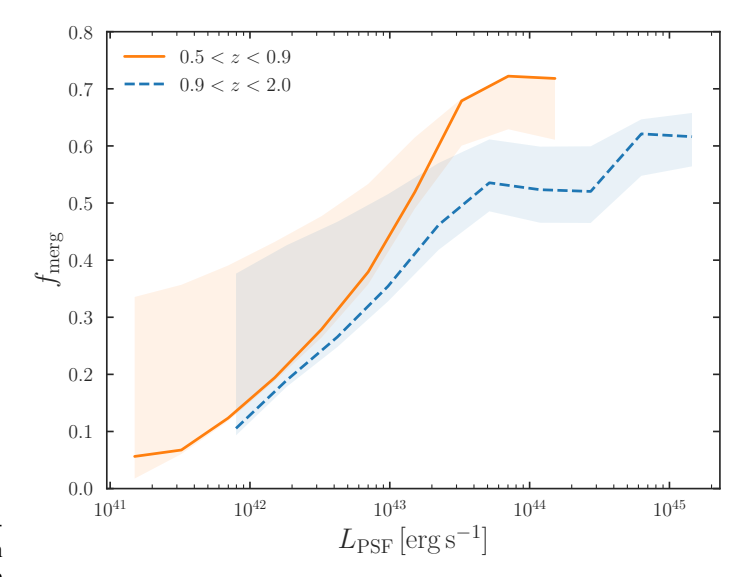


Fig. 17. Monte Carlo simulation of the merger fraction and PSF luminosity relation. The solid line trends reported are the same as in Fig. 12, while the shaded areas represent the full parameter space covered (0th-100th percentile range) by the MC simulation results.

Similarly, we calculated the weighted sum of temporary 'mergers' within the AGN host sample and divided it by the total weighted sum of the AGN host sample. The same was done for the non-AGN control sample, generating distributions for the merger fraction in both populations. Figure 16 illustrates the median $f_{\rm merg}$ from each distribution obtained through the MC simulation, alongside the 2.5th to 97.5th percentile range, divided into two redshift bins. On average, the merger fraction was found to be slightly higher in the AGN samples compared to the non-AGN controls across the MC iterations. However, the parameter space ranges for AGN and non-AGN controls overlap in most cases.

5.3.2. Systematic uncertainties on the $f_{\rm merg}$ - $L_{\rm PSF}$ relation

For each MC iteration, we recalculated $f_{\rm merg}$ in each $L_{\rm PSF}$ bin using the weighted counts. Figure 17 shows that, as expected, the MC simulations yield a broader range of $f_{\rm merg}$ values compared to the bootstrapping uncertainties. The median trend across the 1000 MC iterations closely follows the trend derived directly from the initial classification (solid lines), while the shaded areas (0th-100th percentile range) illustrate the propagated uncertainty. The MC results demonstrate that while uncertainties introduce larger scatter, particularly at lower luminosities ($L_{\rm PSF} < 10^{43}\,{\rm erg\,s^{-1}}$), the rising trend of $f_{\rm merg}$ with increasing $L_{\rm PSF}$ remains robust. The conclusion that mergers dominate ($f_{\rm merg} > 50\%$) among the most luminous AGN holds true across the vast majority of the MC realisations.

In summary, our detailed MC simulations, incorporating the measured precision and recall, indicate that our classifier is sufficiently robust to establish the primary qualitative conclusions presented in Sect. 4. Both the enhanced presence of AGN in mergers found in the binary analysis and the trend of increasing merger importance for more luminous AGN seen in the continuous analysis hold even when accounting for realistic levels of misclassification inherent to automated methods in deep surveys.

6. Summary and conclusions

In this paper, we have performed the first detection of major mergers in the Euclid VIS I_E -band imaging data and examined the merger and AGN connection at $0.5 \le z \le 2.0$ in the Q1 EDFs. We constructed a stellar mass-complete sample of galaxies $(M_{\star} > 10^{9.8} M_{\odot})$ and employed a CNN trained on mock Euclid observations generated from Illustris-TNG simulations to identify merging galaxies. We defined mergers in Illustris-TNG galaxies with a major merger event (a stellar mass ratio ≤ 4) in the time interval spanning 800 Myr before to 300 Myr after coalescence. We exploited the rich multi-wavelength datasets for selecting AGN using four different diagnostics to select AGN via X-ray detections, optical spectroscopy (DESI data), two different MIR colour selections, and a DL-based imaging decomposition technique. We analysed the role of mergers in triggering AGN using a binary approach and a more refined approach that focuses on continuous AGN parameters. Our key findings are the following.

- i) A larger fraction of AGN in mergers than in non-merger controls, which results in an excess of AGN in mergers, regardless of the AGN selection used. X-ray and DL-based AGN show a factor of two to three excess in mergers across the whole redshift range. DESI-selected AGN show a larger excess (3.9) at $z \ge 0.9$ than at z < 0.9 (3.1). MIR AGN show an excess that depends on the criterion adopted. For the more reliable selection, R90, the excess is much larger (a factor of 4.2–4.5) than that of the more complete selection, C75 (1.7). This indicates that mergers can trigger all AGN types but are likely to be more connected with dust-obscured AGN.
- ii) A higher merger fraction (f_{merg}) in active galaxies, with a larger fraction in AGN by 15–25 percentage points compared to non-AGN controls, for all AGN types. However, we cannot conclude with certainty whether mergers are a primary triggering mechanism.
- iii) A rising trend in the $f_{\rm merg}$ as a function of the PSF relative contribution $f_{\rm PSF}$, measured in the $I_{\rm E}$ -band up to $f_{\rm PSF} \simeq 0.55$ followed by a decline. This trend is independent of the redshift. In the range $f_{\rm PSF} = 0.3$ –0.75, most galaxies are classified as mergers, which hints towards a scenario where mergers are the prevalent fuelling mechanism in relatively dominant AGN ($f_{\rm PSF} > 0.5$).
- iv) A positive correlation between $f_{\rm merg}$ and the PSF luminosity, $L_{\rm PSF}$, where mergers represent more than 50% of the galaxies at $L_{\rm PSF} > 10^{43.5}\,{\rm erg\,s^{-1}}$ for z < 0.9 and at $10^{45}\,{\rm erg\,s^{-1}}$ for $z \ge 0.9$. This confirms the idea that mergers are the main channel to fuel the brightest AGN.

Moreover, we performed detailed MC simulations to assess the impact of potential misclassification and incompleteness from our merger identification pipeline. While showing much larger uncertainties, these tests demonstrated that our primary conclusions are qualitatively robust and not driven by classification systematics.

In conclusion, our results prove that mergers are closely linked to relatively dominant and bright AGN. Moreover, larger merger fractions and AGN excesses are observed for MIR AGN, which are usually linked to the dust-obscured phase of AGN lives. This suggests that mergers efficiently funnel gas to the central regions of galaxies, driving rapid accretion onto the SMBH, possibly obscuring it with dust, and making AGN more detectable in the MIR. For less dominant AGN, other fuelling mechanisms may play a more important role. Although mergers appear to be the primary – if not the sole – trigger for the most

luminous AGN at z < 0.9, their influence may decline at higher redshifts, where galaxies typically have larger gas reservoirs capable of sustaining AGN activity without external triggers.

A key limitation of this study is the reliance on CNN-based merger classification, which inherently has accuracy constraints despite being trained on cosmological simulations. While the main trends remain robust, some level of misclassification is unavoidable. Future improvements in classification techniques will be essential to refining merger identification. This study, although based on only 63 deg², highlights the statistical power of Euclid in probing mergers and AGN fuelling. With upcoming Euclid releases, the sample size will increase dramatically, marking a transition from being limited by statistical uncertainties to a regime dominated by systematics, which must be understood to advance the field. Complementary datasets from XMM-Newton, eROSITA, and JWST, as well as ancillary far-IR and radio observations, will further expand the AGN sample, allowing for a more precise assessment of the role of mergers in AGN evolution. Crucially, these data will allow us to map the merger and AGN connection in a multi-dimensional space and simultaneously analyse it as a function of key galaxy properties such as stellar mass, redshift, gas content, star formation rate, and environment.

Acknowledgements. This work has made use of the Euclid Quick Release Q1 data from the Euclid mission of the European Space Agency (ESA), 2025, https://doi.org/10.57780/esa-2853f3b. The Euclid Consortium acknowledges the European Space Agency and a number of agencies and institutes that have supported the development of Euclid, in particular the Agenzia Spaziale Italiana, the Austrian Forschungsförderungsgesellschaft funded through BMK, the Belgian Science Policy, the Canadian Euclid Consortium, the Deutsches Zentrum für Luft- und Raumfahrt, the DTU Space and the Niels Bohr Institute in Denmark, the French Centre National d'Etudes Spatiales, the Fundação para a Ciência e a Tecnologia, the Hungarian Academy of Sciences, the Ministerio de Ciencia, Innovación y Universidades, the National Aeronautics and Space Administration, the National Astronomical Observatory of Japan, the Netherlandse Onderzoekschool Voor Astronomie, the Norwegian Space Agency, the Research Council of Finland, the Romanian Space Agency, the State Secretariat for Education, Research, and Innovation (SERI) at the Swiss Space Office (SSO), and the United Kingdom Space Agency. A complete and detailed list is available on the Euclid web site (www.euclid-ec.org). Based on data from UNIONS, a scientific collaboration using three Hawaii-based telescopes: CFHT, Pan-STARRS, and Subaru www.skysurvey.cc. Based on data from the Dark Energy Camera (DECam) on the Blanco 4-m Telescope at CTIO in Chile https://www.darkenergysurvey.org. This publication is part of the project 'Clash of the titans: deciphering the enigmatic role of cosmic collisions' (with project number VI.Vidi.193.113 of the research programme Vidi which is (partly) financed by the Dutch Research Council (NWO). This research makes use of ESA Datalabs (datalabs.esa.int), an initiative by ESA's Data Science and Archives Division in the Science and Operations Department, Directorate of Science. We thank SURF (www.surf.nl) for the support in using the National Supercomputer Snellius. This research was supported by the International Space Science Institute (ISSI) in Bern, through ISSI International Team project #23-573 'Active Galactic Nuclei in Next Generation Surveys'. This work has benefited from the support of Royal Society Research Grant RGS\R1\231450. FR, VA acknowledge the support from the INAF Large Grant 'AGN & Euclid: a close entanglement' Ob. Fu. 01.05.23.01.14. ALM is grateful for the indispensable discussion with Christopher Boettner and Scott C. Trager.

References

Abadi, M., Agarwal, A., Barham, P., et al. 2016, arXiv e-prints:1603.04467 Aird, J., Coil, A. L., & Georgakakis, A. 2017, MNRAS, 465, 3390 Aird, J., Coil, A. L., Moustakas, J., et al. 2012, ApJ, 746, 90 Alexander, D. M. & Hickox, R. C. 2012, New Astronomy Reviews, 56, 93 Allevato, V., Finoguenov, A., Cappelluti, N., et al. 2011, ApJ, 736, 99 Assef, R. J., Stern, D., Noirot, G., et al. 2018, ApJS, 234, 23 Barnes, J. E. & Hernquist, L. 1996, ApJ, 471, 115 Bianchi, L., Shiao, B., & Thilker, D. 2017, ApJS, 230, 24 Bichang'a, B., Kaviraj, S., Lazar, I., et al. 2024, MNRAS, 532, 613 Bickley, R. W., Ellison, S. L., Patton, D. R., & Wilkinson, S. 2023, MNRAS, 519, 6149

489, 1859

```
Bickley, R. W., Ellison, S. L., Salvato, M., et al. 2024, MNRAS, 533, 3068
Blecha, L., Snyder, G. F., Satyapal, S., & Ellison, S. L. 2018, MNRAS, 478,
Blumenthal, K. A. & Barnes, J. E. 2018, MNRAS, 479, 3952
Bongiorno, A., Merloni, A., Brusa, M., et al. 2012, MNRAS, 427, 3103
Boquien, M., Burgarella, D., Roehlly, Y., et al. 2019, A&A, 622, A103
Bornancini, C. G., Oio, G. A., Alonso, M. V., & García Lambas, D. 2022, A&A,
   664, A110
Bottrell, C., Hani, M. H., Teimoorinia, H., et al. 2019, MNRAS, 490, 5390
Bruzual, G. & Charlot, S. 2003, MNRAS, 344, 1000
Byrne-Mamahit, S., Hani, M. H., Ellison, S. L., Quai, S., & Patton, D. R. 2023,
   MNRAS, 519, 4966
Chollet, F. 2023, Keras, https://keras.io
Cisternas, M., Jahnke, K., Inskip, K. J., et al. 2011, ApJ, 726, 57
Comerford, J. M., Nevin, R., Negus, J., et al. 2024, ApJ, 963, 53
Darg, D. W., Kaviraj, S., Lintott, C. J., et al. 2010, MNRAS, 401, 1552
DESI Collaboration, Abareshi, B., Aguilar, J., et al. 2022, ApJ, 164, 207
DESI Collaboration, Adame, A. G., Aguilar, J., et al. 2024, AJ, 168, 58
DESI Collaboration, Aghamousa, A., Aguilar, J., et al. 2016, arXiv e-
   prints:1611.00036
Dey, A., Schlegel, D. J., Lang, D., et al. 2019, AJ, 157, 168
Di Matteo, T., Croft, R. A. C., Springel, V., & Hernquist, L. 2003, ApJ, 593, 56
Donley, J. L., Kartaltepe, J., Kocevski, D., et al. 2018, ApJ, 853, 63
Draper, A. R. & Ballantyne, D. R. 2012, ApJ, 751, 72
Ellison, S. L., Viswanathan, A., Patton, D. R., et al. 2019, MNRAS, 487, 2491
Euclid Collaboration: Aussel, H., Tereno, I., Schirmer, M., et al. 2025, A&A,
   submitted (Euclid Q1 SI), arXiv:2503.15302
Euclid Collaboration: Bisigello, L., Massimo, M., Tortora, C., et al. 2024, A&A,
   691, A1
Euclid Collaboration: Cropper, M., Al-Bahlawan, A., Amiaux, J., et al. 2025,
   A&A, 697, A2
Euclid Collaboration: Enia, A., Pozzetti, L., Bolzonella, M., et al. 2025,
   A&A, in press (Euclid Q1 SI), https://doi.org/10.1051/0004-6361/
   202554576, arXiv:2503.15314
Euclid Collaboration: Jahnke, K., Gillard, W., Schirmer, M., et al. 2025, A&A,
   697, A3
Euclid Collaboration: Lusso, E., Fotopoulou, S., Selwood, M., et al. 2024, A&A,
   685, A108
Euclid Collaboration: Margalef-Bentabol, B., Wang, L., La Marca, A., et al.
   2025, A&A, submitted (Euclid Q1 SI), arXiv:2503.15318
Euclid Collaboration: Matamoro Zatarain, T., Fotopoulou, S., Ricci, F., et al.
   2025, A&A, submitted (Euclid Q1 SI), arXiv:2503.15320
Euclid Collaboration: McCracken, H. J., Benson, K., Dolding, C., et al. 2025,
   A&A, submitted (Euclid Q1 SI), arXiv:2503.15303
Euclid Collaboration: Mellier, Y., Abdurro'uf, Acevedo Barroso, J., et al. 2025,
   A&A, 697, A1
Euclid Collaboration: Polenta, G., Frailis, M., Alavi, A., et al. 2025, A&A, sub-
   mitted (Euclid Q1 SI), arXiv:2503.15304
Euclid Collaboration: Romelli, E., Kümmel, M., Dole, H., et al. 2025,
   A&A, in press (Euclid Q1 SI), https://doi.org/10.1051/0004-6361/
   202554586, arXiv:2503.15305
Euclid Collaboration: Roster, W., Salvato, M., Buchner, J., et al. 2025, A&A,
   submitted (Euclid Q1 SI), arXiv:2503.15316
Euclid Collaboration: Selwood, M., Fotopoulou, S., Bremer, M. N., et al. 2025,
   A&A, 693, A250
Euclid Collaboration: Tucci, M., Paltani, S., Hartley, W. G., et al. 2025,
   A&A, in press (Euclid Q1 SI), https://doi.org/10.1051/0004-6361/
   202554588, arXiv:2503.15306
Euclid Collaboration: Walmsley, M., Huertas-Company, M., Quilley, L., et al.
   2025, A&A, submitted (Euclid Q1 SI), arXiv:2503.15310
Euclid Quick Release Q1. 2025, https://doi.org/10.57780/esa-2853f3b
Evans, I. N., Evans, J. D., Martínez-Galarza, J. R., et al. 2024, ApJS, 274, 22
Fabian, A. C. 2012, ARA&A, 50, 455
Ferreira, L., Conselice, C. J., Duncan, K., et al. 2020, ApJ, 895, 115
Fritz, J., Franceschini, A., & Hatziminaoglou, E. 2006, MNRAS, 366, 767
Gaia Collaboration, Prusti, T., de Bruijne, J. H. J., et al. 2016, A&A, 595, A1 Gao, F., Wang, L., Pearson, W. J., et al. 2020, A&A, 637, A94
Garland, I. L., Fahey, M. J., Simmons, B. D., et al. 2023, MNRAS, 522, 211
Glikman, E., Simmons, B., Mailly, M., et al. 2015, ApJ, 806, 218
Goulding, A. D., Greene, J. E., Bezanson, R., et al. 2018, PASJ, 70, S37
Grogin, N. A., Conselice, C. J., Chatzichristou, E., et al. 2005, ApJ, 627, L97
Grylls, P. J., Shankar, F., & Conselice, C. J. 2020, MNRAS, 499, 2265
Harrison, C. M., Costa, T., Tadhunter, C. N., et al. 2018, Nature Astronomy, 2,
Heckman, T. M. & Best, P. N. 2014, ARA&A, 52, 589
Hewlett, T., Villforth, C., Wild, V., et al. 2017, MNRAS, 470, 755
Hickox, R. C. & Alexander, D. M. 2018, ARA&A, 56, 625
Hodges, J. L. 1958, Arkiv for Matematik, 3, 469
Hopkins, P. F., Hernquist, L., Cox, T. J., & Kereš, D. 2008, ApJS, 175, 356
```

```
Knapen, J. H., Cisternas, M., & Querejeta, M. 2015, MNRAS, 454, 1742
Kocevski, D. D., Brightman, M., Nandra, K., et al. 2015, ApJ, 814, 104
Kocevski, D. D., Faber, S. M., Mozena, M., et al. 2012, ApJ, 744, 148
Koulouridis, E., Gkini, A., & Drigga, E. 2024, A&A, 684, A111
Koulouridis, E., Plionis, M., Chavushyan, V., et al. 2006, ApJ, 639, 37
La Marca, A., Margalef-Bentabol, B., Wang, L., et al. 2024, A&A, 690, A326
Lackner, C. N., Silverman, J. D., Salvato, M., et al. 2014, ApJ, 148, 137
Laureijs, R., Amiaux, J., Arduini, S., et al. 2011, ESA/SRE(2011)12,
   arXiv:1110.3193
Lecun, Y., Bottou, L., Bengio, Y., & Haffner, P. 1998, Proceedings of the IEEE,
   86, 2278
Li, W., Nair, P., Irwin, J., et al. 2023, ApJ, 944, 168
Marconi, A., Risaliti, G., Gilli, R., et al. 2004, MNRAS, 351, 169
Margalef-Bentabol, B., Wang, L., La Marca, A., et al. 2024a, A&A, 687, A24
Margalef-Bentabol, B., Wang, L., La Marca, A., & Rodriguez-Gomez, V. 2024b,
   arXiv e-prints, arXiv:2410.01437
Marian, V., Jahnke, K., Mechtley, M., et al. 2019, ApJ, 882, 141
Marinacci, F., Vogelsberger, M., Pakmor, R., et al. 2018, MNRAS, 480, 5113
Martin, G., Kaviraj, S., Volonteri, M., et al. 2018, MNRAS, 476, 2801
Merloni, A., Lamer, G., Liu, T., et al. 2024, A&A, 682, A34
Miyazaki, S., Komiyama, Y., Kawanomoto, S., et al. 2018, PASJ, 70, S1
Moreno, J., Torrey, P., Ellison, S. L., et al. 2019, MNRAS, 485, 1320
Mountrichas, G., Buat, V., Georgantopoulos, I., et al. 2021, A&A, 653, A70
Moustakas, J., Scholte, D., Dey, B., & Khederlarian, A. 2023, FastSpecFit: Fast
   spectral synthesis and emission-line fitting of DESI spectra, Astrophysics
   Source Code Library, record ascl:2308.005
Naiman, J. P., Pillepich, A., Springel, V., et al. 2018, MNRAS, 477, 1206
Navarro, V., Del Rio, S., Diego, M. A., et al. 2024, in Space Data Management,
   ed. A. Cortesi, Vol. 141 (Singapore: Springer Nature Singapore), 1-13
Nelson, D., Pillepich, A., Springel, V., et al. 2018, MNRAS, 475, 624
Nevin, R., Blecha, L., Comerford, J., & Greene, J. 2019, ApJ, 872, 76
Nevin, R., Blecha, L., Comerford, J., et al. 2023, MNRAS, 522, 1
Oke, J. B. & Gunn, J. E. 1983, ApJ, 266, 713
Pierce, J. C. S., Tadhunter, C. N., Gordon, Y., et al. 2022, MNRAS, 510, 1163
Pillepich, A., Nelson, D., Hernquist, L., et al. 2018, MNRAS, 475, 648
Pozzetti, L., Bolzonella, M., Zucca, E., et al. 2010, A&A, 523, A13
Predehl, P., Andritschke, R., Arefiev, V., et al. 2021, A&A, 647, A1
Ricci, C., Bauer, F. E., Treister, E., et al. 2017, MNRAS, 468, 1273
Ricci, C., Privon, G. C., Pfeifle, R. W., et al. 2021, MNRAS, 506, 5935
Rodriguez-Gomez, V., Genel, S., Vogelsberger, M., et al. 2015, MNRAS, 449,
Rodriguez-Gomez, V., Snyder, G. F., Lotz, J. M., et al. 2019, MNRAS, 483, 4140
Salvato, M., Buchner, J., Budavári, T., et al. 2018, MNRAS, 473, 4937
Sanders, D. B., Soifer, B. T., Elias, J. H., Neugebauer, G., & Matthews, K. 1988,
   ApJ, 328, L35
Schawinski, K., Treister, E., Urry, C. M., et al. 2011, ApJ, 727, L31
Secrest, N. J., Ellison, S. L., Satyapal, S., & Blecha, L. 2020, MNRAS, 499,
  2380
Shen, X., Hopkins, P. F., Faucher-Giguère, C.-A., et al. 2020, MNRAS, 495,
Silva, A., Marchesini, D., Silverman, J. D., et al. 2021, ApJ, 909, 124
Silverman, J. D., Mainieri, V., Lehmer, B. D., et al. 2008, ApJ, 675, 1025
Siudek, M., Pucha, R., Mezcua, M., et al. 2024, A&A, 691, A308
Smethurst, R. J., Beckmann, R. S., Simmons, B. D., et al. 2024, MNRAS, 527,
Somerville, R. S. & Davé, R. 2015, ARA&A, 53, 51
Springel, V., Di Matteo, T., & Hernquist, L. 2005, MNRAS, 361, 776
Springel, V., Pakmor, R., Pillepich, A., et al. 2018, MNRAS, 475, 676
Springel, V., White, S. D. M., Tormen, G., & Kauffmann, G. 2001, MNRAS,
Tacconi, L. J., Genzel, R., Neri, R., et al. 2010, Nature, 463, 781
Tanaka, M., Koike, M., Naito, S., et al. 2023, PASJ, 75, 986
Taylor, M. B. 2006, in Astronomical Society of the Pacific Conference Se-
   ries, Vol. 351, Astronomical Data Analysis Software and Systems XV, ed.
   C. Gabriel, C. Arviset, D. Ponz, & S. Enrique, 666
The Dark Energy Survey Collaboration. 2005, arXiv e-prints:astro-ph/0510346
Toba, Y., Yamada, S., Matsubayashi, K., et al. 2022, PASJ, 74, 1356
Treister, E., Schawinski, K., Urry, C. M., & Simmons, B. D. 2012, ApJ, 758, L39
Urrutia, T., Lacy, M., & Becker, R. H. 2008, ApJ, 674, 80
Villforth, C. 2023, The Open Journal of Astrophysics, 6, 34
Villforth, C., Hamilton, T., Pawlik, M. M., et al. 2017, MNRAS, 466, 812
Walmsley, M., Allen, C., Aussel, B., et al. 2023, The Journal of Open Source
   Software, 8, 5312
Walmsley, M., Scaife, A. M. M., Lintott, C., et al. 2022, MNRAS, 513, 1581
Wang, L., Pearson, W. J., & Rodriguez-Gomez, V. 2020, A&A, 644, A87
```

Webb, N. A., Coriat, M., Traulsen, I., et al. 2020, A&A, 641, A136

2018, MNRAS, 476, 2308

Weigel, A. K., Schawinski, K., Treister, E., Trakhtenbrot, B., & Sanders, D. B.

Huertas-Company, M., Rodriguez-Gomez, V., Nelson, D., et al. 2019, MNRAS,

- Wright, E. L., Eisenhardt, P. R. M., Mainzer, A. K., et al. 2010, AJ, 140, 1868 Yang, G., Boquien, M., Brandt, W. N., et al. 2022, ApJ, 927, 192 Yang, G., Boquien, M., Buat, V., et al. 2020, MNRAS, 491, 740
- Zanisi, L., Huertas-Company, M., Lanusse, F., et al. 2021, MNRAS, 501, 4359
 - ¹ SRON Netherlands Institute for Space Research, Landleven 12, 9747 AD, Groningen, The Netherlands
 - ² Kapteyn Astronomical Institute, University of Groningen, PO Box 800, 9700 AV Groningen, The Netherlands
 - ³ Department of Physics, Oxford University, Keble Road, Oxford OX1 3RH, UK
 - Department of Physical Sciences, Ritsumeikan University, Kusatsu, Shiga 525-8577, Japan
 - National Astronomical Observatory of Japan, 2-21-1 Osawa, Mitaka, Tokyo 181-8588, Japan
 - ⁶ Academia Sinica Institute of Astronomy and Astrophysics (ASIAA), 11F of ASMAB, No. 1, Section 4, Roosevelt Road, Taipei 10617, Taiwan
 - Institute of Space Sciences (ICE, CSIC), Campus UAB, Carrer de Can Magrans, s/n, 08193 Barcelona, Spain
 - Institut d'Estudis Espacials de Catalunya (IEEC), Edifici RDIT, Campus UPC, 08860 Castelldefels, Barcelona, Spain
 - ⁹ Instituto de Radioastronomía y Astrofísica, Universidad Nacional Autónoma de México, A.P. 72-3, 58089 Morelia, Mexico
 - Department of Mathematics and Physics, Roma Tre University, Via della Vasca Navale 84, 00146 Rome, Italy
 - della Vasca Navale 84, 00146 Rome, Italy

 11 INAF-Osservatorio Astronomico di Roma, Via Frascati 33, 00078
- Monteporzio Catone, Italy
 School of Physics, HH Wills Physics Laboratory, University of
- Bristol, Tyndall Avenue, Bristol, BS8 1TL, UK

 13 INAF-Osservatorio Astronomico di Capodimonte, Via Moiariello
- 16, 80131 Napoli, Italy
 School of Physics & Astronomy, University of Southampton, High-
- field Campus, Southampton SO17 IBJ, UK
- ¹⁵ INAF-Osservatorio Astronomico di Padova, Via dell'Osservatorio 5, 35122 Padova, Italy
- ¹⁶ Instituto de Astrofísica de Canarias (IAC); Departamento de Astrofísica, Universidad de La Laguna (ULL), 38200, La Laguna, Tenerife, Spain
- Max Planck Institute for Extraterrestrial Physics, Giessenbachstr. 1, 85748 Garching, Germany
- ¹⁸ INAF-Istituto di Astrofisica e Planetologia Spaziali, via del Fosso del Cavaliere, 100, 00100 Roma, Italy
- ¹⁹ Department of Physics and Astronomy, University of British Columbia, Vancouver, BC V6T 1Z1, Canada
- ²⁰ Instituto de Astrofísica de Canarias, Vía Láctea, 38205 La Laguna,
- Tenerife, Spain

 21 Universidad de La Laguna, Departamento de Astrofísica, 38206 La
- Laguna, Tenerife, Spain

 22 Sterrenkundig Observatorium, Universiteit Gent, Kriigslaan 281
- Sterrenkundig Observatorium, Universiteit Gent, Krijgslaan 28 S9, 9000 Gent, Belgium
- ²³ ESAC/ESA, Camino Bajo del Castillo, s/n., Urb. Villafranca del Castillo, 28692 Villanueva de la Cañada, Madrid, Spain
- ²⁴ Université Paris-Saclay, CNRS, Institut d'astrophysique spatiale, 91405, Orsay, France
- ²⁵ School of Mathematics and Physics, University of Surrey, Guildford, Surrey, GU2 7XH, UK
- ²⁶ INAF-Osservatorio Astronomico di Brera, Via Brera 28, 20122 Milano, Italy
- ²⁷ INAF-Osservatorio di Astrofisica e Scienza dello Spazio di Bologna, Via Piero Gobetti 93/3, 40129 Bologna, Italy
- ²⁸ Université Paris-Saclay, Université Paris Cité, CEA, CNRS, AIM, 91191, Gif-sur-Yvette, France
- ²⁹ IFPU, Institute for Fundamental Physics of the Universe, via Beirut 2, 34151 Trieste, Italy
- ³⁰ INAF-Osservatorio Astronomico di Trieste, Via G. B. Tiepolo 11, 34143 Trieste, Italy
- 31 INFN, Sezione di Trieste, Via Valerio 2, 34127 Trieste TS, Italy
- 32 SISSA, International School for Advanced Studies, Via Bonomea 265, 34136 Trieste TS, Italy

- ³³ Dipartimento di Fisica e Astronomia, Università di Bologna, Via Gobetti 93/2, 40129 Bologna, Italy
- ³⁴ INFN-Sezione di Bologna, Viale Berti Pichat 6/2, 40127 Bologna, Italy
- 35 Space Science Data Center, Italian Space Agency, via del Politecnico snc, 00133 Roma, Italy
- ³⁶ Dipartimento di Fisica, Università di Genova, Via Dodecaneso 33, 16146, Genova, Italy
- 37 INFN-Sezione di Genova, Via Dodecaneso 33, 16146, Genova, Italy
- ³⁸ Department of Physics "E. Pancini", University Federico II, Via Cinthia 6, 80126, Napoli, Italy
- ³⁹ Instituto de Astrofísica e Ciências do Espaço, Universidade do Porto, CAUP, Rua das Estrelas, PT4150-762 Porto, Portugal
- ⁴⁰ Faculdade de Ciências da Universidade do Porto, Rua do Campo de Alegre, 4150-007 Porto, Portugal
- ⁴¹ Dipartimento di Fisica, Università degli Studi di Torino, Via P. Giuria 1, 10125 Torino, Italy
- ⁴² INFN-Sezione di Torino, Via P. Giuria 1, 10125 Torino, Italy
- ⁴³ INAF-Osservatorio Astrofisico di Torino, Via Osservatorio 20, 10025 Pino Torinese (TO), Italy
- ⁴⁴ European Space Agency/ESTEC, Keplerlaan 1, 2201 AZ Noordwijk, The Netherlands
- ⁴⁵ Institute Lorentz, Leiden University, Niels Bohrweg 2, 2333 CA Leiden, The Netherlands
- ⁴⁶ Leiden Observatory, Leiden University, Einsteinweg 55, 2333 CC Leiden, The Netherlands
- ⁴⁷ INAF-IASF Milano, Via Alfonso Corti 12, 20133 Milano, Italy
- ⁴⁸ Centro de Investigaciones Energéticas, Medioambientales y Tecnológicas (CIEMAT), Avenida Complutense 40, 28040 Madrid, Spain
- ⁴⁹ Port d'Informació Científica, Campus UAB, C. Albareda s/n, 08193 Bellaterra (Barcelona), Spain
- ⁵⁰ INFN section of Naples, Via Cinthia 6, 80126, Napoli, Italy
- ¹ Institute for Astronomy, University of Hawaii, 2680 Woodlawn Drive, Honolulu, HI 96822, USA
- ⁵² Dipartimento di Fisica e Astronomia "Augusto Righi" Alma Mater Studiorum Università di Bologna, Viale Berti Pichat 6/2, 40127 Bologna, Italy
- ⁵³ Institute for Astronomy, University of Edinburgh, Royal Observatory, Blackford Hill, Edinburgh EH9 3HJ, UK
- Jodrell Bank Centre for Astrophysics, Department of Physics and Astronomy, University of Manchester, Oxford Road, Manchester M13 9PL, UK
- European Space Agency/ESRIN, Largo Galileo Galilei 1, 00044 Frascati, Roma, Italy
- Université Claude Bernard Lyon 1, CNRS/IN2P3, IP2I Lyon, UMR 5822, Villeurbanne, F-69100, France
- ⁵⁷ Aix-Marseille Université, CNRS, CNES, LAM, Marseille, France
- ⁵⁸ Institut de Ciències del Cosmos (ICCUB), Universitat de Barcelona (IEEC-UB), Martí i Franquès 1, 08028 Barcelona, Spain
- ⁵⁹ Institució Catalana de Recerca i Estudis Avançats (ICREA), Passeig de Lluís Companys 23, 08010 Barcelona, Spain
- ⁶⁰ UCB Lyon 1, CNRS/IN2P3, IUF, IP2I Lyon, 4 rue Enrico Fermi, 69622 Villeurbanne, France
- Mullard Space Science Laboratory, University College London, Holmbury St Mary, Dorking, Surrey RH5 6NT, UK
- ⁶² Departamento de Física, Faculdade de Ciências, Universidade de Lisboa, Edifício C8, Campo Grande, PT1749-016 Lisboa, Portugal
- 63 Instituto de Astrofísica e Ciências do Espaço, Faculdade de Ciências, Universidade de Lisboa, Campo Grande, 1749-016 Lisboa, Portugal
- ⁶⁴ Department of Astronomy, University of Geneva, ch. d'Ecogia 16, 1290 Versoix, Switzerland
- ⁶⁵ Aix-Marseille Université, CNRS/IN2P3, CPPM, Marseille, France
- ⁶⁶ Universitäts-Sternwarte München, Fakultät für Physik, Ludwig-Maximilians-Universität München, Scheinerstrasse 1, 81679 München, Germany
- ⁶⁷ INFN-Bologna, Via Irnerio 46, 40126 Bologna, Italy

- ⁶⁸ FRACTAL S.L.N.E., calle Tulipán 2, Portal 13 1A, 28231, Las Rozas de Madrid, Spain
- ⁶⁹ Dipartimento di Fisica "Aldo Pontremoli", Università degli Studi di Milano, Via Celoria 16, 20133 Milano, Italy
- ⁷⁰ INFN-Sezione di Milano, Via Celoria 16, 20133 Milano, Italy
- NRC Herzberg, 5071 West Saanich Rd, Victoria, BC V9E 2E7, Canada
- ⁷² Institute of Theoretical Astrophysics, University of Oslo, P.O. Box 1029 Blindern, 0315 Oslo, Norway
- ⁷³ Jet Propulsion Laboratory, California Institute of Technology, 4800 Oak Grove Drive, Pasadena, CA, 91109, USA
- ⁷⁴ Department of Physics, Lancaster University, Lancaster, LA1 4YB, UK
- ⁷⁵ Felix Hormuth Engineering, Goethestr. 17, 69181 Leimen, Germany
- ⁷⁶ Technical University of Denmark, Elektrovej 327, 2800 Kgs. Lyngby, Denmark
- ⁷⁷ Cosmic Dawn Center (DAWN), Denmark
- ⁷⁸ Institut d'Astrophysique de Paris, UMR 7095, CNRS, and Sorbonne Université, 98 bis boulevard Arago, 75014 Paris, France
- Max-Planck-Institut für Astronomie, Königstuhl 17, 69117 Heidelberg, Germany
- NASA Goddard Space Flight Center, Greenbelt, MD 20771, USA
- ⁸¹ Department of Physics and Astronomy, University College London, Gower Street, London WC1E 6BT, UK
- 82 Department of Physics and Helsinki Institute of Physics, Gustaf Hällströmin katu 2, 00014 University of Helsinki, Finland
- ⁸³ Université de Genève, Département de Physique Théorique and Centre for Astroparticle Physics, 24 quai Ernest-Ansermet, CH-1211 Genève 4, Switzerland
- ⁸⁴ Department of Physics, P.O. Box 64, 00014 University of Helsinki, Finland
- 85 Helsinki Institute of Physics, Gustaf Hällströmin katu 2, University of Helsinki, Helsinki, Finland
- Rentre de Calcul de l'IN2P3/CNRS, 21 avenue Pierre de Coubertin 69627 Villeurbanne Cedex, France
- ⁸⁷ Laboratoire d'etude de l'Univers et des phenomenes eXtremes, Observatoire de Paris, Université PSL, Sorbonne Université, CNRS, 92190 Meudon, France
- ⁸⁸ SKA Observatory, Jodrell Bank, Lower Withington, Macclesfield, Cheshire SK11 9FT, UK
- ⁸⁹ University of Applied Sciences and Arts of Northwestern Switzerland, School of Computer Science, 5210 Windisch, Switzerland
- ⁹⁰ Universität Bonn, Argelander-Institut für Astronomie, Auf dem Hügel 71, 53121 Bonn, Germany
- 91 INFN-Sezione di Roma, Piazzale Aldo Moro, 2 c/o Dipartimento di Fisica, Edificio G. Marconi, 00185 Roma, Italy
- ⁹² Dipartimento di Fisica e Astronomia "Augusto Righi" Alma Mater Studiorum Università di Bologna, via Piero Gobetti 93/2, 40129 Bologna, Italy
- ⁹³ Department of Physics, Institute for Computational Cosmology, Durham University, South Road, Durham, DH1 3LE, UK
- ⁹⁴ Université Côte d'Azur, Observatoire de la Côte d'Azur, CNRS, Laboratoire Lagrange, Bd de l'Observatoire, CS 34229, 06304 Nice cedex 4, France
- ⁹⁵ Université Paris Cité, CNRS, Astroparticule et Cosmologie, 75013 Paris, France
- ONRS-UCB International Research Laboratory, Centre Pierre Binetruy, IRL2007, CPB-IN2P3, Berkeley, USA
- ⁹⁷ University of Applied Sciences and Arts of Northwestern Switzerland, School of Engineering, 5210 Windisch, Switzerland
- ⁹⁸ Institut d'Astrophysique de Paris, 98bis Boulevard Arago, 75014, Paris, France
- ⁹⁹ Institute of Physics, Laboratory of Astrophysics, Ecole Polytechnique Fédérale de Lausanne (EPFL), Observatoire de Sauverny, 1290 Versoix, Switzerland
- Aurora Technology for European Space Agency (ESA), Camino bajo del Castillo, s/n, Urbanizacion Villafranca del Castillo, Villanueva de la Cañada, 28692 Madrid, Spain

- ¹⁰¹ Institut de Física d'Altes Energies (IFAE), The Barcelona Institute of Science and Technology, Campus UAB, 08193 Bellaterra (Barcelona), Spain
- Oschool of Mathematics, Statistics and Physics, Newcastle University, Herschel Building, Newcastle-upon-Tyne, NE1 7RU, UK
- DARK, Niels Bohr Institute, University of Copenhagen, Jagtvej 155, 2200 Copenhagen, Denmark
- Waterloo Centre for Astrophysics, University of Waterloo, Waterloo, Ontario N2L 3G1, Canada
- Department of Physics and Astronomy, University of Waterloo, Waterloo, Ontario N2L 3G1, Canada
- Perimeter Institute for Theoretical Physics, Waterloo, Ontario N2L 2Y5, Canada
- 107 Centre National d'Etudes Spatiales Centre spatial de Toulouse, 18 avenue Edouard Belin, 31401 Toulouse Cedex 9, France
- ¹⁰⁸ Institute of Space Science, Str. Atomistilor, nr. 409 Măgurele, Ilfov, 077125, Romania
- 109 Consejo Superior de Investigaciones Cientificas, Calle Serrano 117, 28006 Madrid, Spain
- Dipartimento di Fisica e Astronomia "G. Galilei", Università di Padova, Via Marzolo 8, 35131 Padova, Italy
- ¹¹¹ INFN-Padova, Via Marzolo 8, 35131 Padova, Italy
- ¹¹² Caltech/IPAC, 1200 E. California Blvd., Pasadena, CA 91125, USA
- ¹¹³ Institut für Theoretische Physik, University of Heidelberg, Philosophenweg 16, 69120 Heidelberg, Germany
- Institut de Recherche en Astrophysique et Planétologie (IRAP), Université de Toulouse, CNRS, UPS, CNES, 14 Av. Edouard Belin, 31400 Toulouse, France
- ¹¹⁵ Université St Joseph; Faculty of Sciences, Beirut, Lebanon
- Departamento de Física, FCFM, Universidad de Chile, Blanco Encalada 2008, Santiago, Chile
- ¹¹⁷ Universität Innsbruck, Institut für Astro- und Teilchenphysik, Technikerstr. 25/8, 6020 Innsbruck, Austria
- Satlantis, University Science Park, Sede Bld 48940, Leioa-Bilbao, Spain
- ¹¹⁹ Infrared Processing and Analysis Center, California Institute of Technology, Pasadena, CA 91125, USA
- ¹²⁰ Instituto de Astrofísica e Ciências do Espaço, Faculdade de Ciências, Universidade de Lisboa, Tapada da Ajuda, 1349-018 Lisboa, Portugal
- ¹²¹ Cosmic Dawn Center (DAWN)
- Niels Bohr Institute, University of Copenhagen, Jagtvej 128, 2200 Copenhagen, Denmark
- Universidad Politécnica de Cartagena, Departamento de Electrónica y Tecnología de Computadoras, Plaza del Hospital 1, 30202 Cartagena, Spain
- Dipartimento di Fisica e Scienze della Terra, Università degli Studi di Ferrara, Via Giuseppe Saragat 1, 44122 Ferrara, Italy
- 125 Istituto Nazionale di Fisica Nucleare, Sezione di Ferrara, Via Giuseppe Saragat 1, 44122 Ferrara, Italy
- ¹²⁶ INAF, Istituto di Radioastronomia, Via Piero Gobetti 101, 40129 Bologna, Italy
- ¹²⁷ Université PSL, Observatoire de Paris, Sorbonne Université, CNRS, LERMA, 75014, Paris, France
- ¹²⁸ Université Paris-Cité, 5 Rue Thomas Mann, 75013, Paris, France
- ¹²⁹ INAF Osservatorio Astronomico di Brera, via Emilio Bianchi 46, 23807 Merate, Italy
- ¹³⁰ INAF-Osservatorio Astronomico di Brera, Via Brera 28, 20122 Milano, Italy, and INFN-Sezione di Genova, Via Dodecaneso 33, 16146, Genova, Italy
- ¹³¹ ICL, Junia, Université Catholique de Lille, LITL, 59000 Lille, France
- ¹³² ICSC Centro Nazionale di Ricerca in High Performance Computing, Big Data e Quantum Computing, Via Magnanelli 2, Bologna, Italy
- ¹³³ Instituto de Física Teórica UAM-CSIC, Campus de Cantoblanco, 28049 Madrid, Spain
- ¹³⁴ CERCA/ISO, Department of Physics, Case Western Reserve University, 10900 Euclid Avenue, Cleveland, OH 44106, USA

- Technical University of Munich, TUM School of Natural Sciences, Physics Department, James-Franck-Str. 1, 85748 Garching, Germany
- Max-Planck-Institut für Astrophysik, Karl-Schwarzschild-Str. 1, 85748 Garching, Germany
- Laboratoire Univers et Théorie, Observatoire de Paris, Université PSL, Université Paris Cité, CNRS, 92190 Meudon, France
- Departamento de Física Fundamental. Universidad de Salamanca. Plaza de la Merced s/n. 37008 Salamanca, Spain
- ¹³⁹ Université de Strasbourg, CNRS, Observatoire astronomique de Strasbourg, UMR 7550, 67000 Strasbourg, France
- ¹⁴⁰ Center for Data-Driven Discovery, Kavli IPMU (WPI), UTIAS, The University of Tokyo, Kashiwa, Chiba 277-8583, Japan
- ¹⁴¹ Ludwig-Maximilians-University, Schellingstrasse 4, 80799 Munich, Germany
- Max-Planck-Institut für Physik, Boltzmannstr. 8, 85748 Garching, Germany
- ¹⁴³ Dipartimento di Fisica Sezione di Astronomia, Università di Trieste, Via Tiepolo 11, 34131 Trieste, Italy
- California Institute of Technology, 1200 E California Blvd, Pasadena, CA 91125, USA
- 145 Department of Physics & Astronomy, University of California
- Irvine, Irvine CA 92697, USA

 146 Department of Mathematics and Physics E. De Giorgi, University
- of Salento, Via per Arnesano, CP-I93, 73100, Lecce, Italy

 147 INFN, Sezione di Lecce, Via per Arnesano, CP-193, 73100, Lecce,

 Italy
- Italy

 INAF-Sezione di Lecce, c/o Dipartimento Matematica e Fisica, Via
- per Arnesano, 73100, Lecce, Italy

 Departamento Física Aplicada, Universidad Politécnica de Carta-
- gena, Campus Muralla del Mar, 30202 Cartagena, Murcia, Spain
 150 Instituto de Física de Cantabria, Edificio Juan Jordá, Avenida de los Castros, 39005 Santander, Spain
- 151 CEA Saclay, DFR/IRFU, Service d'Astrophysique, Bat. 709, 91191 Gif-sur-Yvette France
- 91191 Gif-sur-Yvette, France

 152 Institute of Cosmology and Gravitation, University of Portsmouth,
- Portsmouth PO1 3FX, UK

 153 Department of Computer Science, Aalto University, PO Box 15400, Espoo, FI-00 076, Finland
- Instituto de Astrofísica de Canarias, c/ Via Lactea s/n, La Laguna 38200, Spain. Departamento de Astrofísica de la Universidad de La Laguna, Avda. Francisco Sanchez, La Laguna, 38200, Spain
- Ruhr University Bochum, Faculty of Physics and Astronomy, Astronomical Institute (AIRUB), German Centre for Cosmological Lensing (GCCL), 44780 Bochum, Germany
- Department of Physics and Astronomy, Vesilinnantie 5, 20014 University of Turku, Finland
- 157 Serco for European Space Agency (ESA), Camino bajo del Castillo, s/n, Urbanizacion Villafranca del Castillo, Villanueva de la Cañada, 28692 Madrid, Spain
- ARC Centre of Excellence for Dark Matter Particle Physics, Melbourne, Australia
- ¹⁵⁹ Centre for Astrophysics & Supercomputing, Swinburne University of Technology, Hawthorn, Victoria 3122, Australia
- Department of Physics and Astronomy, University of the Western Cape, Bellville, Cape Town, 7535, South Africa
- DAMTP, Centre for Mathematical Sciences, Wilberforce Road, Cambridge CB3 0WA, UK
- Kavli Institute for Cosmology Cambridge, Madingley Road, Cambridge, CB3 0HA, UK
- Department of Astrophysics, University of Zurich, Winterthurerstrasse 190, 8057 Zurich, Switzerland
- Department of Physics, Centre for Extragalactic Astronomy, Durham University, South Road, Durham, DH1 3LE, UK
- ¹⁶⁵ Institute for Theoretical Particle Physics and Cosmology (TTK), RWTH Aachen University, 52056 Aachen, Germany
- ¹⁶⁶ IRFU, CEA, Université Paris-Saclay 91191 Gif-sur-Yvette Cedex, France
- Oskar Klein Centre for Cosmoparticle Physics, Department of Physics, Stockholm University, Stockholm, SE-106 91, Sweden

- Astrophysics Group, Blackett Laboratory, Imperial College London, London SW7 2AZ, UK
- ¹⁶⁹ Univ. Grenoble Alpes, CNRS, Grenoble INP, LPSC-IN2P3, 53, Avenue des Martyrs, 38000, Grenoble, France
- ¹⁷⁰ INAF-Osservatorio Astrofisico di Arcetri, Largo E. Fermi 5, 50125, Firenze, Italy
- ¹⁷¹ Dipartimento di Fisica, Sapienza Università di Roma, Piazzale Aldo Moro 2, 00185 Roma, Italy
- Centro de Astrofísica da Universidade do Porto, Rua das Estrelas, 4150-762 Porto, Portugal
- ¹⁷³ HE Space for European Space Agency (ESA), Camino bajo del Castillo, s/n, Urbanizacion Villafranca del Castillo, Villanueva de la Cañada, 28692 Madrid, Spain
- 174 Department of Astrophysical Sciences, Peyton Hall, Princeton University, Princeton, NJ 08544, USA
- ¹⁷⁵ Theoretical astrophysics, Department of Physics and Astronomy, Uppsala University, Box 515, 751 20 Uppsala, Sweden
- Minnesota Institute for Astrophysics, University of Minnesota, 116 Church St SE, Minneapolis, MN 55455, USA
- 177 Mathematical Institute, University of Leiden, Einsteinweg 55, 2333 CA Leiden, The Netherlands
- ¹⁷⁸ Institute of Astronomy, University of Cambridge, Madingley Road, Cambridge CB3 0HA, UK
- ¹⁷⁹ Department of Physics and Astronomy, University of California, Davis, CA 95616, USA
- Space physics and astronomy research unit, University of Oulu, Pentti Kaiteran katu 1, FI-90014 Oulu, Finland
- ¹⁸¹ Center for Computational Astrophysics, Flatiron Institute, 162 5th Avenue, 10010, New York, NY, USA



Fig. A.1. Confusion matrix comparing our model predictions with the Zoobot classifications. Along the diagonal, we report the precision (orange) and the recall (red) of each class. In black, the number of galaxies in each cell. Results are averaged over ten different balanced sets.

Appendix A: Comparison with Zoobot classification

We compared the predictions of the model trained in this work with the classification given by the Zoobot model (Euclid Collaboration: Walmsley et al. 2025) for the subsample of galaxies in common. We used two Zoobot catalogue columns to identify mergers, the merging merger fraction and the merging major-disturbance fraction, which allow us to select both pair galaxies and highly disturbed post-merging galaxies. As a first step, we removed possible artefacts from the Zoobot catalogue by setting problem artifact fraction < 0.01 AND problem star fraction < 0.01 AND problem $zoom\ fraction < 0.01$. Then, we defined the mergers as those galaxies with merging merger fraction > 0.7 OR merging major-disturbance fraction > 0.5, and the nonmergers as merging merger fraction < 0.2 AND merging major-disturbance fraction < 0.1. We chose these criteria in order to obtain pure samples of mergers and non-mergers. In total, we found 40 847 galaxies in common. Of these, 27.8% are unclassified according to our model classification, which we removed to compare merger and non-merger classifications.

We created balanced samples of the Zoobot mergers and non-mergers by randomly selecting the same number of mergers among the available non-mergers. This operation was repeated ten times, and we report the average results in Fig. A.1. Our model has a precision of 71% and 86% for mergers and non-mergers, respectively, when compared to the Zoobot labels. Compared to the performance on the TNG test set, we observed a lower precision for the merger class, but an improved precision for the non-mergers. At the same time, our model classification is highly complete with respect to Zoobot mergers, with a recall of 90%, but has a much lower recall for the non-mergers, 63%. Overall, the F1-scores for both classes are the same as for the TNG test set. Considering all Zoobot mergers in the common subsample, our model classifies as mergers 90% of them (75%)

if we do not exclude unclassified galaxies), demonstrating good agreement between our classification and labels obtained from a model trained on visual classification.

We visually inspected the cases where Zoobot and our CNN disagree. We observed that sometimes Zoobot misclassified mergers picked up by our CNN, but also the opposite is true (i.e., our CNN misclassified mergers correctly labelled by Zoobot). Nevertheless, we note that the comparison between our classifier and Zoobot is inherently dependent on the choice of classification thresholds in both approaches. Variations in these thresholds can significantly affect the reported merger fractions and the relative performance of the methods.

The performance of our CNN, when compared to Zoobot labels as shown in Fig. A.1, yields precision and recall values for the merger class broadly consistent with the performance achieved by our CNN on the TNG test set (Table 2). These figures, are also comparable to the typical performance levels reported for other state-of-the-art DL methods applied to merger classification in similar large, deep surveys (Margalef-Bentabol et al. 2024a). This consistency suggests that the level of accuracy, and the associated inherent uncertainties (as discussed in Sect. 5.3), are characteristic of current methodologies rather than specific shortcomings of our individual classifier.

Appendix B: Example of unclassified galaxies

We show some randomly sampled examples of unclassified galaxies in Fig. B.1. Unclassified galaxies are those objects with a predicted score between 0.35 and 0.59, inclusive. These unclassified objects appear as intermediate between mergers and non-mergers. While some look isolated and undisturbed, others appear to have close neighbours and an irregular morphology.

Appendix C: AGN sample: Additional information

We show the various intersections of all AGN selection methods used in this work in Fig. C.1 as an UpSet plot. This plot displays intersections in a matrix, with rows corresponding to the AGN selections and columns representing the intersections between these sets. The size of the sets and the intersections are shown as bar charts. The DL-based method correctly identifies about 25–30% of DESI, X-ray, and R90 MIR-selected AGN, while only about 10% of C75 MIR AGN. Relaxing the $f_{\rm PSF} \geq 0.2$ constraint to 0.1, the DL-based model recognises many more AGN (Fig. C.2): it correctly identifies > 50% of DESI, X-ray and R90 AGN, and about 25% of C75 AGN. It is not surprising that the C75 selection method has the lowest identification ratio, as this diagnostic is also the most contaminated one.

Figure C.3 shows the normalised redshift distributions of all AGN types. X-ray and DESI AGN mostly inhabit z < 1 galaxies, with very few individuals at higher redshift. MIR AGN, both the C75 and the R90 selections, on average have higher redshifts, with their distributions peaking at $z \simeq 1$. DL-selected AGN mostly follow the same z distribution of the full galaxy sample, which has its maximum at $z \simeq 0.7$ and then monotonically decreases towards higher redshifts. This behaviour is expected because the DL-based AGN population strongly depends on the original population of galaxies.

Appendix D: $f_{ m merg}$ as a function of $f_{ m PSF}$ and $L_{ m PSF}$ for individual AGN selections

Here, we analyse the relation of the merger fraction with the point source fraction and luminosity for individual AGN selec-



Fig. B.1. Examples of galaxies that we label as unclassified. The cutouts are *Euclid* RGB composite images, $8'' \times 8''$, generated as in Fig. 3.

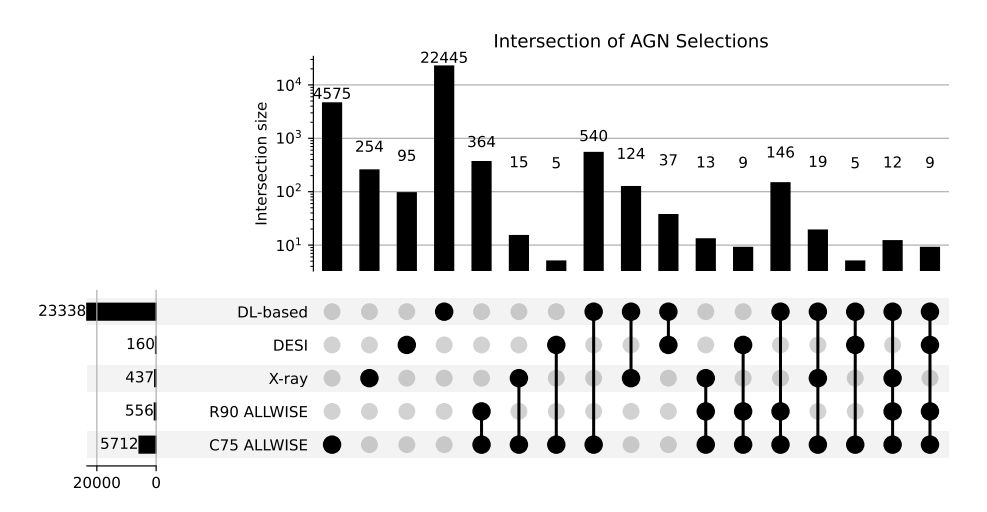


Fig. C.1. UpSet plot showing the intersections of all AGN selection methods employed. Rows correspond to the AGN selections, while columns correspond to the intersections. Numbers of each selection and intersection are displayed as bar charts. Intersections with fewer than five elements are not shown to facilitate readability.

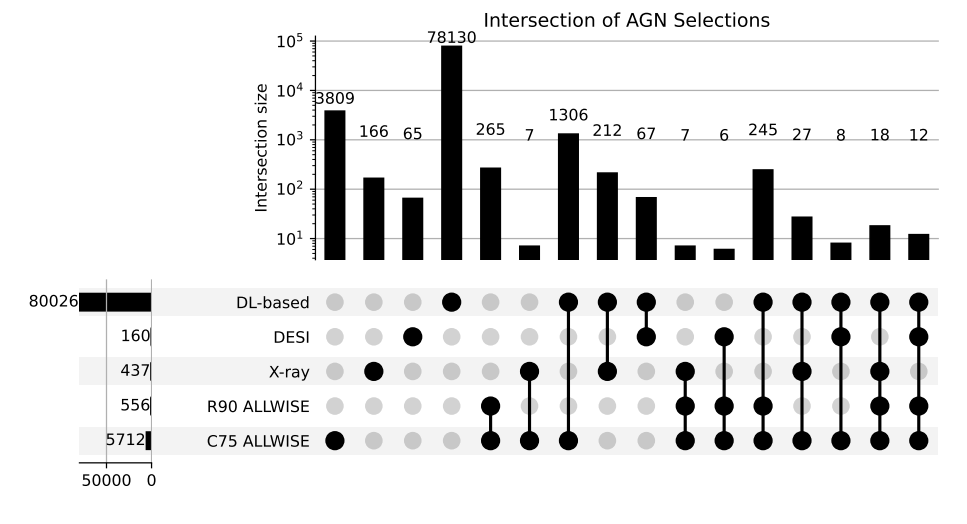


Fig. C.2. UpSet plot showing the intersections of all AGN selection methods employed but with DL-based AGN defined as $f_{\rm PSF} \geq 0.1$, as in Fig. C.1.

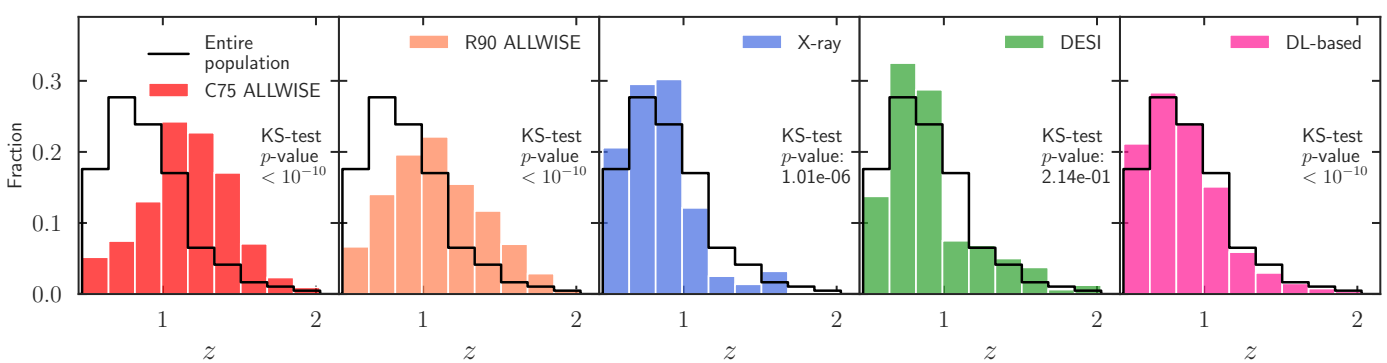


Fig. C.3. Normalised redshift distribution for each AGN population. We overlay the distribution for the entire sample of galaxies and report the results of a KS test in each panel.

Article number, page 24 of 25

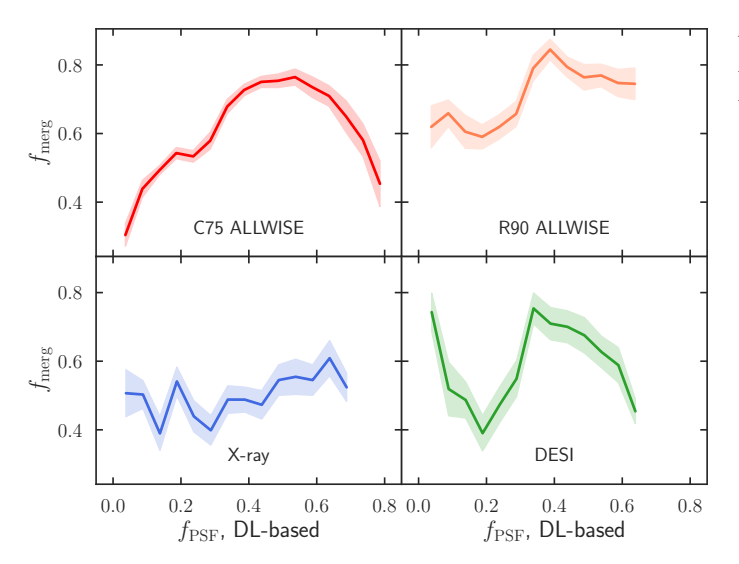


Fig. D.1. Merger fraction and PSF fraction relationship for each AGN type. Trend lines represent the running median, while shaded areas are one standard deviation. The AGN type is indicated in each panel.

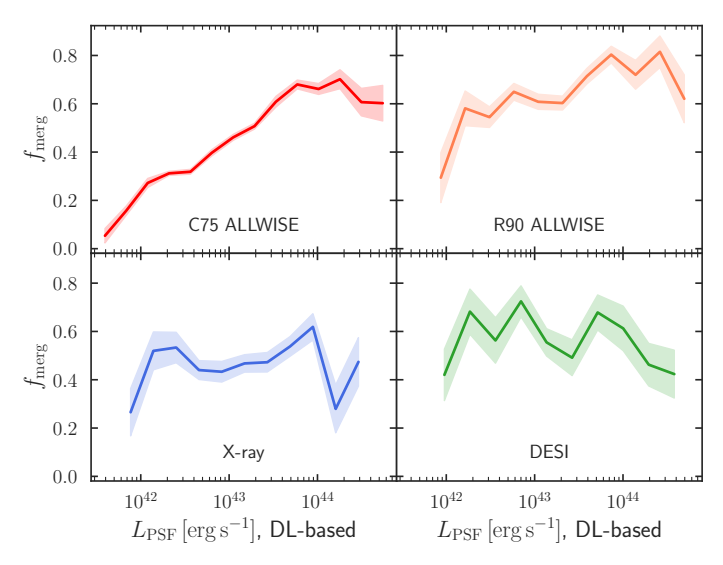


Fig. D.2. Merger fraction and L_{PSF} relation for each AGN type. Trend lines represent the running median, while shaded areas are one standard deviation. The AGN type is indicated in each panel.

tions, to study possible differences. We show the $f_{\rm merg}$ and $f_{\rm PSF}$ relation for X-ray, DESI, and MIR colour selections in Fig. D.1. X-ray and DESI AGN show larger fluctuations, mainly due to fewer objects compared to MIR and DL-based AGN selections. X-ray AGN show a rather flat trend, with a mild increase of $f_{\rm merg}$ as a function of $f_{\rm PSF}$. Regarding the MIR AGN, the R90-selected objects show a rising $f_{\rm merg}$ trend with increasing $f_{\rm PSF}$, centred at very high $f_{\rm merg}$ values (> 0.6). The C75-selected AGN have a trend similar to that of the general population reported in Fig. 9: a sharp rise in $f_{\rm merg}$ up to $f_{\rm PSF} \simeq 0.55$, followed by a decreasing merger fraction.

Likewise, we show the merger fraction and point source luminosity relations for the individual AGN selections in Fig. D.2. X-ray and DESI AGN have a rather flat trend, around $f_{\rm merg} \simeq 0.5$ and $f_{\rm merg} \simeq 0.6$, respectively. Although their trends are significantly different from those in Fig. 12, mergers appear as a dominant fuelling mechanism for both selections. On the other hand, both MIR colour selections show monotonic rising $f_{\rm merg}$ as a function of $L_{\rm PSF}$, with mergers becoming dominant for the

brightest point sources ($L_{\rm PSF} > 10^{43.5}~{\rm erg~s^{-1}}$). In this case, the trends reported are similar to those of the general AGN population in Fig. 12.